Newsletters on Stratigraphy, Vol. 00/0 (0000), 000–000
Published online May 2026

Open Access
Early Access Article

The stratigraphic record of the Eocene–Oligocene transition in the East Pisco Basin (Peru): a phytoplankton perspective

Maria Elena Gastaldello[1], Giulia Bosio[1,2,*], Claudio Di Celma[3], Giovanni Bianucci[2], Alberto Collareta[2], Stefano Mazzoli[3], Luca Pellegrino[4], Igor Maria Villa[1], Mario Urbina[5] and Elisa Malinverno[1]

With 8 figures, 1 table and 2 electronic supplements

Abstract. The East Pisco Basin of southern Peru is renowned worldwide for its exceptionally well-preserved marine vertebrate fossils, recovered from sedimentary successions spanning the middle Eocene to the early Pliocene. Although the lower Eocene–Oligocene deposits of the Otuma Formation have been extensively investigated, the uppermost Eocene to lower Oligocene strata remain comparatively understudied. Notably, these strata encompass the Eocene–Oligocene transition (~ 34 Ma), a critical interval characterized by profound global climatic and ecological changes. This study presents an integrated biostratigraphic analysis of the Otuma Formation based on calcareous nannofossils, diatoms, and silicoflagellates. The investigated deposits were laid down in two distinct sub-basins: an eastern, land-proximal sub-basin at Cerro Tiza and a western, more distal sub-basin at Quebrada Perdida (Media Luna). In addition, ^{39}Ar–^{40}Ar dating of a volcanic ash layer provides an independent chronological tie point for the age model at Cerro Tiza. At both localities, the Otuma Formation comprises calcareous siltstones and diatomite layers deposited from the Priabonian to the Rupelian. Sedimentation rates derived from the age model average 75.5 m/My at Cerro Tiza and 8.1 m/My at Media Luna. A progressive shift from calcareous nannofossil-dominated assemblages to diatom-dominated assemblages throughout the sections reflects a general trend toward cooler conditions and increased nutrient availability, consistent with global patterns during this interval. However, diatom assemblages do not indicate the establishment of permanently eutrophic conditions. Differences in microfossil assemblages, together with an order-of-magnitude contrast in sedimentation rates between Cerro Tiza and Media Luna, point to markedly distinct palaeoenvironmental conditions in the two sub-basins. These differences are interpreted as the result of tectonic controls and contrasting positions within the Peruvian forearc system.

Keywords. Otuma Formation; EOT; diatoms; calcareous nannofossils; global change

Author's addresses:
[1] Dipartimento di Scienze Dell'Ambiente e Della Terra, Università degli Studi di Milano-Bicocca, Milano, Italia
[2] Dipartimento di Scienze della Terra, Università di Pisa, Pisa, Italia
[3] Scuola di Scienze e Tecnologie, Università di Camerino, Camerino, Italia
[4] Dipartimento di Scienze della Terra, Università di Torino, Torino, Italia
[5] Departamento de Paleontología de Vertebrados, Museo de Historia Natural-UNMSM, Lima, Peru
* Corresponding author: giulia.bosio.giulia@gmail.com

© 2026 The Authors

DOI: 10.1127/nos/0873 Borntrager Science Publishers, Stuttgart, www.borntraeger-cramer.de

1. Introduction

The late Eocene to early Oligocene time frame marks one of the most critical intervals of the Cenozoic, one that was characterized by remarkable climatic and ecological changes during the Eocene-Oligocene transition (hereinafter, EOT), a phase of accelerated climatic and biotic change lasting ca. 790 kyr across the Eocene-Oligocene boundary, ~ 34 Ma (Hutchinson et al. 2021). The EOT is marked by a two-step positive shift in deep-sea $\delta^{18}O$ (Shackleton & Kennett, 1975; Kennett & Shackleton 1976; Zachos et al. 1996; Coxall et al. 2005), which is interpreted as representing a combination of deep-ocean cooling and increasing continental ice volume (Lear et al. 2008). At the same time, several independent proxies indicate that the ocean surface seawater also underwent cooling (Lear et al. 2008; Evans et al. 2016; Wade et al. 2012), and major floral and faunal changes worldwide exhibit a shift toward more temperate and cold-adapted biotas (Prothero & Berggren 1992). Also associated with the EOT are: a widespread aridification of the terrestrial ecosystems; a major fall of sea level; the reorganization of deep ocean currents; a major perturbation of the carbon cycle, with a drop in atmospheric CO_2 concentrations and a deepening of the deep-sea carbonate compensation depth; and profound changes in the oceanic phytoplankton, with the rise of diatoms (Cervato & Burckle 2003; Coxall & Pearson 2007; Coxall et al. 2005; Egan et al. 2013; Hutchinson et al. 2021; Miller et al. 2009; Bryłka et al. 2024). Overall, the EOT represents a well-defined, relatively short-lived time interval that witnessed the transition from the late Eocene warmhouse to the early Oligocene coolhouse (Westerhold et al. 2020), as evidenced by the first evidence of a large-scale glaciation of Antarctica (Miller

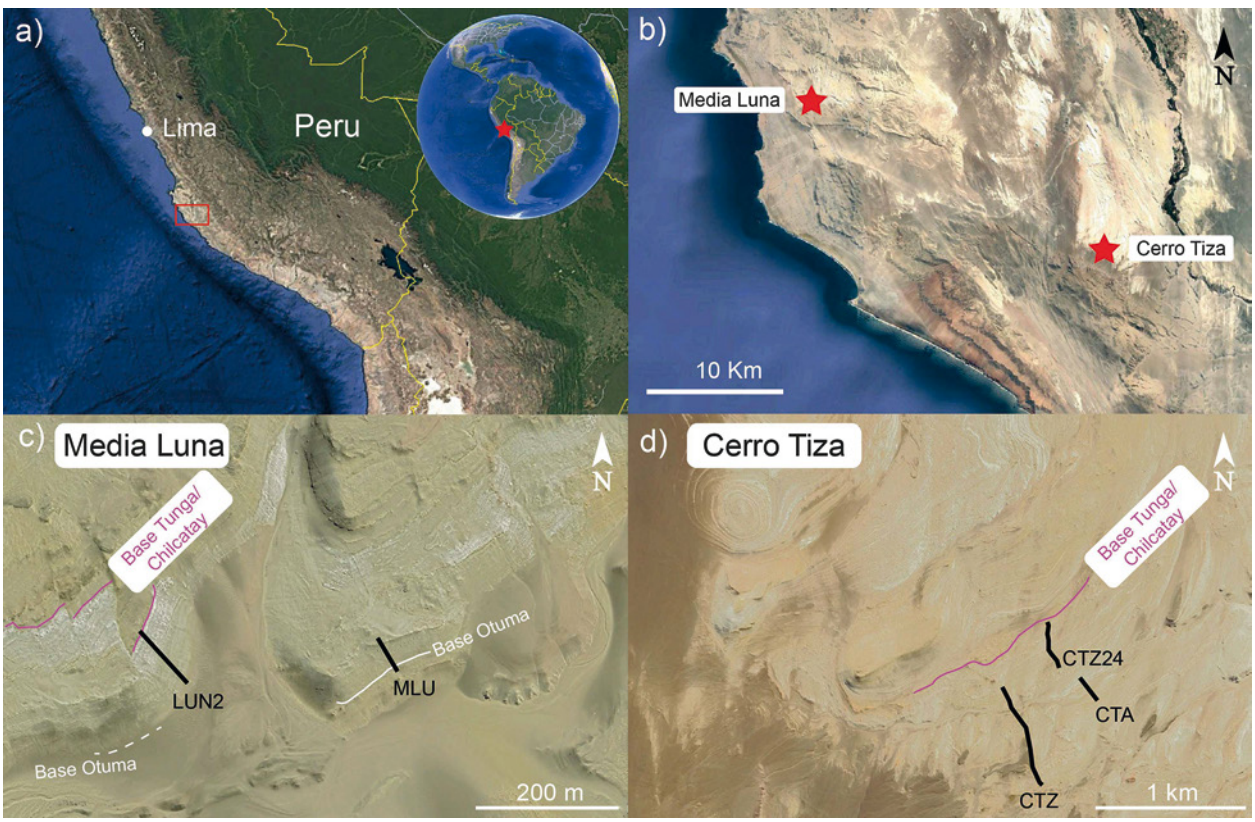

Fig. 1. a) Location map of the EPB (red box); **b)** Location of the two localities, Cerro Tiza (CTZ) and Quebrada Perdida at Media Luna (LUN); **c)** Aerial view from Google Earth of the measured sections at Media Luna (LUN 2 Base: 14°34'02.7''S – 75°53'50.8''W; LUN 2 Top: 14°34'00.4''S – 75°53'52.9''W; MLU Base: 14°34'04.8''S – 75°53'42.7''W; MLU Top: 14°34'00.5''S – 75°53'41.5''W); **d)** Aerial view from Google Earth of the measured sections at Cerro Tiza (CTZ Base: 14°40'51.7''S – 75°40'22.5''W; CTZ Top: 14°40'18.7''S – 75°40'28.6''W; CTZ24 Base: 14°40'27.0'' S – 75°40'18.3''W; CTZ24 Top: 14°40'05.3''S – 75°40'24.6''W; CTA Base: 14°40'34.8''S – 75°40'09.7''W; CTA Top: 14°40'25.5''S – 75°40'15.8''W).

et al. 1991; Pälike et al. 2006; Coxall & Pearson 2007; Zachos et al. 2008; Hutchinson et al. 2021).

The East Pisco Basin (hereinafter, EPB) of southern Peru is broadly recognized as a Fossil-Lagerstätte due to the exceptional abundance and remarkable preservation of its marine vertebrate fossils, which are found within a sedimentary succession spanning the middle Eocene to the Late Miocene, and possibly extending into the Early Pliocene (Gariboldi et al. 2015; Lambert et al. 2015; Bianucci et al. 2016; Bosio et al. 2021; Collareta et al. 2021). The focus of the present study is on the upper Eocene – lower Oligocene Otuma Formation, whose remarkable fossil record provides an exceptional perspective on the late Paleogene evolutionary history of cetaceans and seabirds against the background of major planetary changes (Clarke et al. 2007; Ksepka et al. 2008; Martínez-Cáceres & de Muizon 2011; Uhen et al. 2011; Martínez-Cáceres et al. 2017; Bianucci & Collareta 2022). While the Eocene sedimentary record of the EPB has been extensively documented to date, the Oligocene remains poorly constrained, the only available data being limited to a few scattered samples from a handful of localities, which mostly reveal the occurrence of key diatom markers such as *Azpeitia oligocenica*, *Rhizosolenia oligocenica* and *Rouxia obesa* (DeVries et al. 2017, 2021). However, the exact position of the Eocene-Oligocene boundary and the thickness of the Oligocene sediments at these localities is still unknown. In order to address this knowledge gap, our study investigates the two localities of Cerro Tiza (hereinafter, CTZ) and Quebrada Perdida at Media Luna (hereinafter, LUN), where the Otuma Formation is well exposed. To establish a reliable biostratigraphic framework based on calcareous nannofossils, diatom and silicoflagellates, the Otuma strata were sampled in a systematic and continuous way, with a resolution ranging between 1.5 to 3.0 m.

The aim of the present work is to pinpoint the Eocene – Oligocene Boundary (EOB) along these two sections. This assessment is crucial in order to provide: (i) a reliable stratigraphic basis for future quantitative studies on the response of phytoplanktonic communities to local environmental changes associated with the EOT; (ii) a quantification of sedimentation rates, and particularly their variation, in different domains of the Peruvian forearc system; and (iii) a substantially improved stratigraphic framework constraining the tectonic regime that controlled the evolution of the EPB during the Paleogene.

2. Geological setting

The EPB is one of the NW-SE oriented trench-parallel forearc basins that developed between the middle Eocene and the Early Pliocene along the Peruvian convergent margin (e.g., Fildani et al. 2008; Lajo-Yáñez et al. 2024; Baby et al. 2025) (Fig. 1). The basin history is complex and includes long-term tectonic subsidence (Viveen & Schlunegger 2018), generally attributed to subduction erosion processes (von Huene & Lallemand 1990; von Huene & Suess 1988; Clift et al. 2003; Clift & Vannucchi 2004; Stern 2011), alternating with episodes of forearc crustal shortening and uplift possibly driven by plate coupling. The EPB is bounded to the northeast by the Coastal Batholith and to the southwest by the Outer Shelf High–Coastal Cordillera (Romero et al. 2013), which separates the EPB from the submerged West Pisco Basin (WPB).

The sedimentary fill of the EPB (Fig. 1) is widely exposed in the coastal desert between the towns of Pisco and Nazca (Dunbar et al. 1990; DeVries 1998; León et al. 2008) due to a phase of exhumation attributed to the subduction of the aseismic Nazca Ridge beneath this part of the Peruvian forearc during the Plio-Quaternary (Hsu 1992; Macharé & Ortlieb 1992; Saillard et al. 2011; Ayala-Carazas et al. 2026). The stratigraphic record of the EPB includes a Paleogene and a Neogene megasequence (Di Celma et al. 2022), separated by a major unconformity that marks a basin-wide depositional hiatus spanning the late Oligocene and the earliest Miocene. Such interval of erosion/non-deposition in the EPB corresponds to an interval of major basin uplift, probably related to the Aymara phase (late Oligocene, 28–26 Ma) of Andean orogeny (Herbozo et al. 2020 and references therein).

The Paleogene megasequence consists of the unconformity-bounded middle – upper Eocene Paracas Formation and upper Eocene – lower Oligocene Otuma Formation (Dunbar et al. 1990; DeVries 1998; DeVries et al. 2017; Coletti et al. 2019; Malinverno et al. 2021). The Neogene megasequence includes the unconformity-bounded lower Miocene Tunga Formation (DeVries et al. 2024), lower Miocene Chilcatay Formation (DeVries & Jud 2018; Di Celma et al. 2018a) and middle Miocene to Pliocene Pisco Formation (Dunbar et al. 1990; DeVries 1998; Di Celma et al. 2017, 2018b; Malinverno et al. 2025).

This study examines the Otuma Formation as recorded in two different depocenters of the basin (Fig. 1): the section at Cerro Tiza (CTZ) represents the southwestern deeper portion of the EPB, while the

section at Quebrada Perdida valley in the area of Media Luna (LUN) represents the sediment fill of a minor, roughly W-E-oriented half-graben currently exposed on the Coastal Cordillera. The extensional basin hosting the Otuma Formation is exposed in the study area thanks to the later tectonic uplift of the Coastal Cordillera, which occurred after the Eocene extensional phase (Quispe et al. 2018).

3. Materials and methods

3.1 Sample collection

Geological mapping of the Otuma Formation was carried out at two localities, Cerro Tiza (CTZ) and Quebrada Perdida at Media Luna (LUN), during field campaigns between 2018 and 2024.

In the field, the base of the Otuma Formation is marked by a basal sandstone layer (as described by DeVries 1998; DeVries et al. 2017), which often weathers into characteristic meter-sized spherical concretions. An angular unconformity marks the base of the overlying Tunga or Chilcatay Formation and is typically characterized by a boulder layer and, in some areas, by the presence of phosphate nodules (e.g., Di Celma et al. 2017, 2022; Bosio et al. 2024). In the field, we identified additional marker beds whose lateral extent across the study area provided reliable control for correlation of the Otuma strata. They mainly consist of decimeter-thick indurated layers that can also be easily identified in high-resolution Google Earth images.

Two composite stratigraphic sections exposing the Otuma Formation (Fig. 1) were measured at the two localities (Fig. 2), at a decimeter-scale resolution, using a Jacob's staff equipped with a laser pointer (Patacci 2016). The height is referred to meters above the base of the study section (m). Sediment samples for biostratigraphic purposes were collected at 1.5 to 3 m resolution while measuring the sections, resulting in a total of 124 samples at CTZ and 51 at LUN, as reported in Table S1. Tephra layers were also sampled along the section avoiding weathered and extraneous particles.

3.2 Biostratigraphy

All samples were prepared using the "smear slides" standard method (Bown & Young 1998), using standard rectangular cover slips (22 × 40 mm). Samples were examined using an Olympus BX50 light microscope at 1000× magnification with immersion oil at both parallel and crossed nicols. Three longitudinal transects were analyzed across the slide to detect marker taxa, increasing the number of transects for looking for the rarer ones.

The presence and relative abundance of calcareous nannofossils, diatoms, and silicoflagellates were evaluated for each sample and recorded in a table (Table S1). In order to estimate the total abundance of each group in relation to the remaining sediment, we applied the categories defined by Koç & Scherer (1996): D = dominant, > 60%; A = abundant, 20–60%; C = common, 5–20%; F = few, 2–5%; R = rare, < 2%; B = barren. The relative abundance of each species within each group was estimated per field of view (FOV) or transect on the slide, as: A = abundant; > 10/FOV; C = common; 1–10/FOV; F = few; 1/10 FOVs; R = rare; ≥ 3/transect; VR = 1/transect; Fragments (for diatoms, presence of broken valves); B = barren.

Microfossil preservation in the studied material ranges from moderate (M) to bad (B). Under moderate conditions, calcareous nannofossils show signs of dissolution, yet most diagnostic features remain discernible, while diatoms typically retain frustule rims despite slight dissolution or breakage, with fragments dominating over intact specimens. In contrast, bad preservation is characterized by strongly degraded nannofossil morphologies and by diatom frustules that are dissolved and frequently broken. Silicoflagellates consistently display moderate preservation, with partly broken specimens in most cases.

Calcareous nannofossil species identification follows the taxonomy of Perch-Nielsen (1985a) and the taxonomic database of Young et al. (2024). Diatom species identification follows an extended taxonomy (Jousé 1973; Gombos 1976; Fenner 1978, 1984, 1985, 1991; Barron & Baldauf 1995; Sims et al. 1989; Harwood & Bohaty 2001; Strelnikova et al. 2001; Barron

Fig. 2. Composite stratigraphic sections of CTZ and LUN, position of the identified bioevents, and panoramic photos of the measured outcrops. The stratigraphic intervals of the sampled sections (CTA, CTZ, CTZ24, MLU, LUN2) are indicated on the left, along with the placement of the Eocene – Oligocene Boundary (EOB), as resulting from the age model. Sample height and bioevent identification are shown in Table S1.

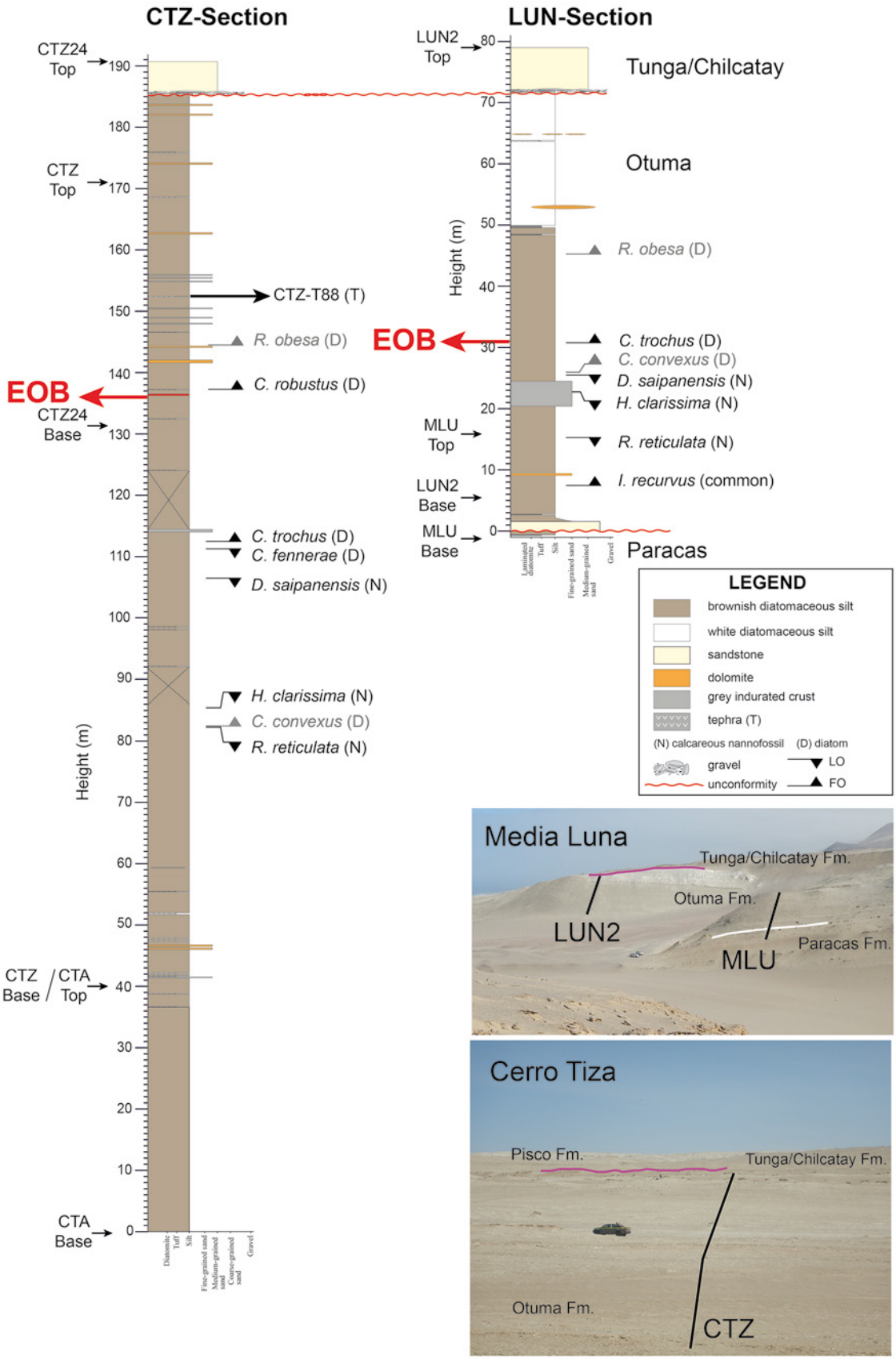
CTZ-Section
LUN-Section
CTZ24 Top
CTZ Top
CTZ-T88 (T)
R. obesa (D)
EOB
C. robustus (D)
CTZ24 Base
C. trochus (D)
C. fennerae (D)
D. saipanensis (N)
H. clarissima (N)
C. convexus (D)
R. reticulata (N)
Height (m)
CTZ Base / CTA Top
CTA Base
LUN2 Top
Tunga/Chilcatay
Otuma
R. obesa (D)
EOB
C. trochus (D)
C. convexus (D)
D. saipanensis (N)
H. clarissima (N)
MLU Top
R. reticulata (N)
I. recurvus (common)
LUN2 Base
MLU Base
Paracas
LEGEND
brownish diatomaceous silt
white diatomaceous silt
sandstone
dolomite
grey indurated crust
tephra (T)
(N) calcareous nannofossil
(D) diatom
gravel
LO
unconformity
FO
Media Luna
Tunga/Chilcatay Fm.
Otuma Fm.
LUN2
MLU
Paracas Fm.
Cerro Tiza
Pisco Fm.
Tunga/Chilcatay Fm.
Otuma Fm.
CTZ

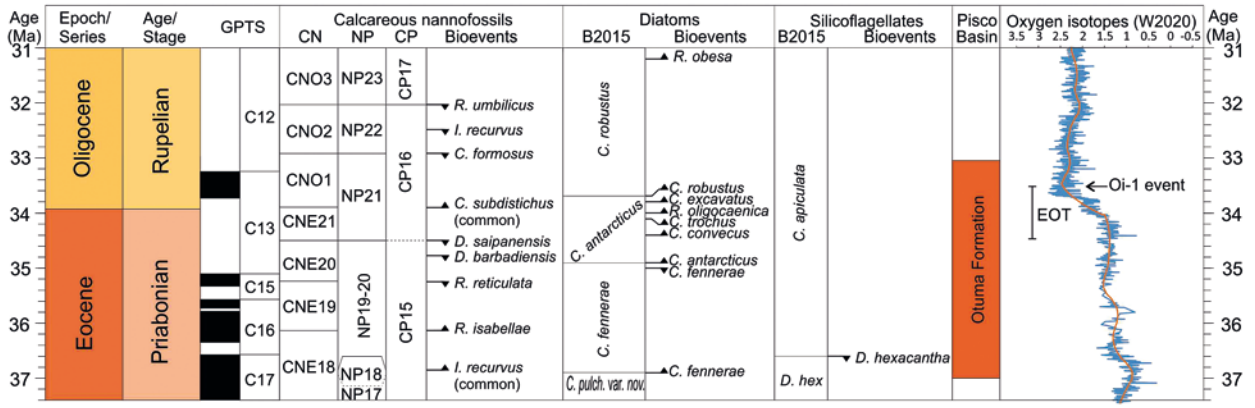

Fig. 3. Biostratigraphic zonal schemes, bioevents and paleoclimatic framework for the late Eocene – early Oligocene interval of the Otuma Formation, plotted with Time Scale Creator using the GPTS2020 and slightly modified. Calcareous nannofossils zones: CN (Agnini et al. 2014), NP (Martini 1971), CP (Okada & Bukry 1980); diatom zones after Fenner et al. (1985) and Barron et al. (2014) with bioevent calibration from Barron et al. (2015); silicoflagellate zones correlated to diatom zones following Barron et al. (2015); global benthic oxygen isotope curve from Westerhold et al. (2020).

et al. 2004, 2014; Scherer et al. 2007; Oreshkina & Radinova 2014) including both Tropical and Southern Ocean species, reflecting the influence of cold Antarctic waters carried northward by the Humboldt Current into tropical regions. The identification of silicoflagellate species follows Bukry (1981, 1987); Barron et al. (1984, 2014); Perch-Nielsen (1985b); Bolli et al. (1989); McCartney et al. (2020).

3.3 Tephra dating

The ash material of sample CTZ-T88 was prepared following the procedures described in Bosio et al. (2019). Grain-size analyses were performed on the selected tephra through the Malvern Mastersizer 2000E™ Laser Granulometer at the Università di Milano-Bicocca. Grain- size data were elaborated with the Grain Size Analysis Program GRADISTAT (Blott & Pye 2001). The ash was wet-sieved using mesh sizes of 500, 250, 125, and 63 µm. The 250–125 µm fraction was embedded in resin, polished, and analyzed for composition with a JEOL 8200 Superprobe at the Università degli Studi di Milano Statale, employing an accelerating voltage of 15 kV and a beam current of 5 nA. Analytical conditions included a beam diameter of 3 µm for biotite phenocrysts and 10 µm for volcanic glass shards. Biotite phenocrysts were subsequently handpicked and irradiated at the McMaster University nuclear reactor. Noble gas isotopic analyses were carried out by step-heating with a NuInstruments Noblesse mass spectrometer at the Università degli Studi di Milano-Bicocca and calculated following established procedures from Bosio et al. (2020a, b).

3.4 Age model and identification of the EOT

The biochronologic data used in this study are related to different microfossil groups: diatoms (Lazarus et al. 2014; Barron et al. 2015; DeVries 2017; Coenen et al. 2025), calcareous nannofossils (Perch-Nielsen 1985a; Agnini et al. 2014; Young et al. 2024), and silicoflagellates (Bukry 1981; Barron et al. 2014, 2015; McCartney et al. 2020). The age ranges of diatom species considered in our biostratigraphic analysis are according to the most recent available references. The relevant bioevents for the time-interval considered in this work and the related zonal schemes were plotted with Time Scale Creator (Fig. 3) and slightly modified.

Table 1 provides the list of bioevents identified in this work, the uncertainty in height along the section, the uncertainty in age determination and the calibration to the Geological Time Scale. The following criteria were considered in order to select the reliable bioevents: the species showed a continuous record along the sections; the sample in which the bioevents were identified are not surrounded by barren intervals. The bioevents meeting these criteria were used as tie points for developing an age model for the Otuma Formation at the two localities. The discarded bioevents are listed in the table but not used in the age model.

Table 1. List of bioevents for the late Eocene – early Oligocene interval, stratigraphic height of occurrence along the studied sections and comment on their reliability. Bioevents identified along the sections but not used in the age model are indicated in grey. Age sources: L14 (Lazarus et al. 2014); A14 (Agnini et al. 2014); B15 (Barron et al. 2015); P85 (Perch-Nielsen et al. 1985); Y25 (Young et al. 2024). Reference Time Scales: G04 (Gradstein et al. 2004); P06 (Pälike et al. 2006); G12 (Gradstein et al. 2012) ; G20 (Gradstein & Ogg, 2020).

						CTZ section							LUN section						
Type	Bioevent	Age (Ma)	Age Err (Ma)	Age Source	Reference Time Scale	Sample Top	Sample Bottom	Depth Top (m)	Depth Bottom (m)	Depth midpoint (m)	Depth Err (m)	Notes	Sample Top	Sample Bottom	Depth Top (m)	Depth Bottom (m)	Depth midpoint (m)	Depth Err (m)	Notes
D	FO *Rouxia obesa*	31.20		L14	G04	CTZ24-D10	CTZ-80	144.90	143.90	144.40	0.50	This species ocours much earlier: DeVries et al. (2017) suggest its FO at 33.8 Ma	LUN2-D59	LUN2-D58	46.00	44.50	45.25	0.75	This species ocours much earlier: DeVries et al. (2017) suggest its FO at 33.8 Ma
N	LO *R. umbilicus*	32.02		A14	P06	CTZ24-D29	CTZ24-D28	174.20	172.80	173.50	0.70	This event is followed by barren samples	LUN2-D55	LUN2-D54	40.00	38.50	39.25	0.75	This event is followed by barren samples
N	LO *I. recurvus*	32.47	0.45	P85		CTZ24-D22	CTZ-100	163.60	162.00	162.80	0.80	This event is followed by barren samples	LUN2-D55	LUN2-D54	40.00	38.50	39.25	0.75	This event is followed by barren samples
N	LO *C. formosus*	32.92		A14	P06	CTZ24-D26	CTZ24-D22	169.90	163.60	166.75	3.15	This event is followed by barren samples	LUN2-D76	LUN2-D75	71.5	70	70.75	0.75	This event is followed by barren samples
D	FO *C. robustus*	33.70		B15	G12	CTZ24-D6	CTZ-75	138.80	137.50	138.15	0.65	This species is often very rare or sometimes absent, so the detection of this bioevent can be not accurate							This species was not observed along the section
D	FO *C. excavatus*	33.80		B15	G12							This species was not observed along the section							This species was not observed along the section
N	FCO *C. subdistichus*	33.88		A14	P06							This species was never observed along the section							This species was not observed along the section
D	FO *R. oligocaenica*	34.00		B15	G12							This species was not observed along the section							This species was not observed along the section
D	FO *C. trochus*	34.10		C25	C20	CTZ-59	CTZ-58	113.00	111.50	112.25	0.75	This species is often very rare, so the detection of this bioevent can be not accurate	LUN2-D49	LUN2-D48	31.00	29.50	30.25	0.75	This species is often very rare, so the detection of this bioevent can be not accurate
D	FO *C. convexus*	34.40		B15	G12	CTZ-38	CTZ-37	83.00	81.50	82.25	0.75	This species is often absent, so the detection of this bioevent might be not accurate	LUN2-D46	LUN2-D45	26.50	25.00	25.75	0.75	This species is often absent, so the detection of this bioevent can be not accurate
N	LO *D. saipanensis*	34.44		A14	P06	CTZ24-D3	CTZ-54	134.20	105.50	119.85	14.35	This bioevent occurs within an interval of barren samples, so it has a high vertical uncertainty	LUN2-D46	LUN2-D45	26.50	25.00	25.75	0.75	This species is often very rare or absent, so detection of this bioevent can be not accurate
N	LO *D. barbadiensis*	34.77		A14	P06							This species was never observed along the section							This species was never observed along the section
D	FO *C. antarcticus*	34.90		B15	G12							This speces was not observed along the section							This speces was not observed along the section
D	LO *C. fennerae*	35.00		B15	G12	CTZ-58	CTZ-57	111.50	110.00	110.75	0.75	This species was often rare							This speces was not observed along the section
N	LO *R. reticulata*	35.24		A14	P06	CTZ-38	CTZ-37	83.00	81.50	82.25	0.75	This species was rare alomg the section	LUN2-D39	LUN2-D38	16.00	14.50	15.25	0.75	This species is sometimes absent close to its last occurrence
N	LO *H. clarissima*	35.71	1.27	Y25		CTZ-43	CTZ-39	93.00	84.50	88.75	4.25	Although diachronous (and thus not commonly used as a bioevent), this event is well recognised along this section	LUN2-D44	LUN2-D43	23.50	22.00	22.75	0.75	Although diachronous (and thus not commonly used as a bioevent), this event is well recognised along this section
N	FO *R. isabellae*	36.13		A14	P06							This species was never observed along the section							Only one specimen was observed along the section
S	LO *D. hecacantha*	36.60		B14	G04														
N	FCO *I.recurvus*	36.84		A14	P06							This species is already present at the base of the measured section	MLU-D8	MLU-D7	7.80	4.70	6.25	1.55	This bioevent is preceded by two barren samples
D	FO *C. fennerae*	36.9		B15	G12							This species, although scattered, is already present at the base of the measured section							

For the CTZ section, the radiometric age was also used as a tie point in the age model. The average linear sedimentation rate (LSR, m/My) was calculated for both sections considering the line of best fit in the age model. The stratigraphic position of the EOB (33.9 Ma) was inferred from the age model for the two sections and shown in Fig. 2.

4. Results

4.1 CTZ-Section

The CTZ-section (Fig. 2) consists of 183.2 m of brownish to pinkish to white-weathered silt, with intercalated volcanic tephra and decimeter-sized dolomite layers. The silt is formed by variable proportions of lithogenic and biogenic grains, with the biogenic component including both calcareous and siliceous microfossils. Several volcanic ash layers have been observed, described and collected; one of these, CTZ-T88, has been selected for microanalytical analyses and radiometric dating.

Calcareous nannofossils are present mainly in the lowermost 84.5 m (CTA-D2 to CTZ-39) of the study section, with abundances ranging from very rare to abundant. In the middle and upper parts, most samples are barren, with only a few short intervals where nannofossils occur (104.0 to 107.0 m and 155.2 to 163.6 m). Diatoms are generally common to abundant throughout the CTZ-section, displaying the highest diversity in the middle portion of the section (65.5 to 125.5 m, CTZ-26 to CTZ-65). Silicoflagellates are generally rare and sporadic throughout most of the section, except for its uppermost portion, where their presence is more continuous (between 158.0 to 183.2 m, CTZ-96 to CTZ24-D35). The ebridian species *Ebriopsis crenulata* and species incertae sedis *Macrora stella* are documented in a few samples along the section.

4.1.1 Calcareous nannofossils

The calcareous nannofossil assemblages at the CTZ-section are primarily dominated, in order of abundance, by *Reticulofenestra, Coccolithus, Discoaster, Sphenolithus, Helicosphaera, Pontosphaera, Blackites, Isthmolithus, Zygrhablithus, Micrantholithus, Chiasmolithus*, and *Coronocyclus*.

Reticulofenestra is the most abundant genus, mainly represented by *R. bisecta*, *R. dictyoda*, and *R. umbilicus*. *Reticulofenestra bisecta* (FO at 40.40 Ma) is the most abundant species in the CTZ-section, closely followed by *R. dictyoda*. Both species exhibit a generally similar abundance throughout most of the samples wherever calcareous nannofossils are present. *Reticulofenestra reticulata* (FO at 42.37 Ma, LO 35.2 Ma; Agnini et al. 2014) ranges from very rare to common and is present up to 81.5 m (CTZ-37), where its last occurrence along the studied section is identified. *Reticulofenestra umbilicus* (FO 43.06 Ma, LO at 32.02 Ma, Agnini et al. 2014) is continuously present along the section, ranging from very rare to common. It occurs up to 172.8 m (CTZ24-D28), above which the samples are barren. *Discoaster saipanensis* (LO 34.44 Ma) is present in the CTZ-section, but it is rare in abundance and highly sporadic. Its last occurrence has been tentatively placed at 105.5 m (CTZ-54), marking the base of the EOT. *Helicosphaera carissima* (LO 35.71 ± 1.27 Ma, Young et al. 2024) occurs as very rare to few and has been documented in the lower part of the interval, up to 84.5 m (sample CTZ-39). *Isthmolithus recurvus* (FO 36.8 Ma, LO 32.47 ± 0.45 Ma; Young et al. 2024) is very rare to rare in abundance and has been documented from the base of the section up to 162.0 m (sample CTZ-100), after which the samples are barren. Finally, *Chiasmolithus oamaruensis*, (FO at 37.84 Ma, LO at 32.47 ± 0.45 Ma; Perch-Nielsen 1985a) has been documented, although very rare, from the base of the section up to 161.0 m (CTZ-98).

4.1.2 Diatoms

The diatom assemblage at the CTZ-section is very diverse and includes, in order of abundance, *Stephanopyxis, Pyxilla, Hemiaulus, Melosira, Rhizosolenia, Coscinodiscus, Paralia, Azpeitia, Actinoptychus, Ces-*

Fig. 4. Diatoms from the Otuma Formation: **1)** *Azpeitia tubercolata/oligocenica* transitional form (CTZ-17); **2)** *Cestodiscus fennerae* (CTZ-63); **3)** *Cestodiscus reticulatus* (CTZ24-D33); **4)** *Cestodiscus convexus* (CTZ-58); **5)** *Cestodiscus robustus* (CTZ-106); **6)** *Cestodiscus* sp. 2 sensu Fenner (CTZ24-D29); **7)** *Cestodiscus trochus* (CTZ-106); **8)** *Cestodiscus* aff. *intersectus* (CTZ-28); **9)** *Hemiaulus altus* (CTZ-09); **10)** *Hemiaulus polycystiunorum* (CTZ-51); **11)** *Hemiaulus subacutus* (CTZ-62); **12)** *Hemiaulus subacutus* with basal constrictions (CTZ-58); **13)** *Stephanopyxis* sp. (CTZ-39); **14)** *Rhizosolenia* sp. (CTZ-81). Scale bar = 10 µm for all images.

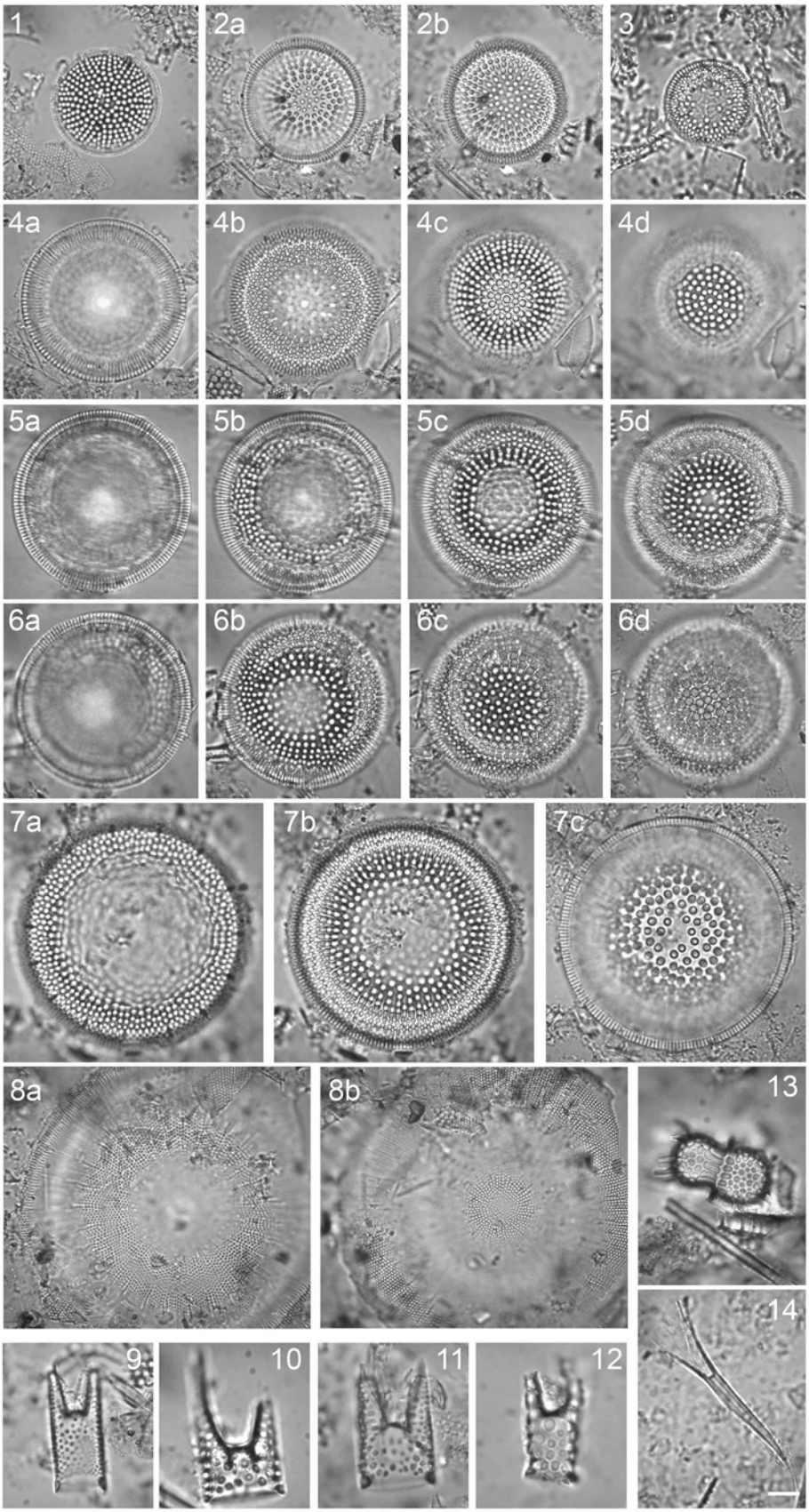
1
2a
2b
3
4a
4b
4c
4d
5a
5b
5c
5d
6a
6b
6c
6d
7a
7b
7c
8a
8b
13
14
9
10
11
12

todiscus, Sceptroneis, Triceratium, Thalassionema, Arachnoidiscus, Rhaphoneis, Rouxia, Actinocyclus, Pterotheca, and *Asterolampra*,

Chaetoceros resting spores occur persistently throughout the study interval ranging from very rare to common. *Stephanopyxis* and *Coscinodiscus* are both very rare to abundant and maintain a consistent presence throughout the CTZ-section. *Hemiaulus* is continuously present along the section. The most abundant species in this genus are middle Eocene to early Oligocene *Hemiaulus polycystinorum* (Fenner, 1978; Fig. 4.10) and late Paleocene to early Oligocene *Hemiaulus subacutus* (FO 57.1 Ma Barron et al. 2015, LO 30.1 Ma Lazarus et al. 2014; Fig. 4.11), both species ranging from very rare to common. Specimens of *H. subacutus* with basal constrictions, typical of the early Oligocene (Fenner 1985; Fig. 4.12), as well as *Hemiaulus altus* (Fig. 4.9) and *Hemiaulus grassus* (FO 45.1, LO 36.0 Ma, Lazarus et al. 2014), have been documented from the base of the section up to sample 137.5 m (CTZ-75). Their presence is discontinuous. When present, their abundance ranges from very rare to few.

Rhizosolenia (Fig. 4.14) is present throughout the section, with abundance ranging from very rare to rare up to 133.0 m (sample CTZ-71), then from few to common. *Pyxilla* first appears around 48.5 m (sample CTZ-12) and remains particularly abundant (few to abundant) up to sample 156.5 m (CTZ-94) before decreasing in the uppermost part of the section. It is represented by middle Eocene to early Oligocene *Pyxilla reticulata* (FO 46.4 Ma, LO 30.9 Ma, Lazarus et al. 2014) (Fig. 6.1, 6.2), also including *P. johnsoniana*, now considered as one of its varieties, (Fig. 6.3). *Azpeitia* ranges from very rare to common and is found throughout most of the CTZ-section, although becoming scattered in the upper 30 m. *Azpeitia tubercolata/oligocenica* transitional form (FO 37 Ma, LO 33.9 Ma, Barron et al. 2014; Fig. 4.1) is the most abundant species of this genus up to 125.5 m (CTZ-65), ranging from very rare to common, while rare *A. oligocenica* (FO 34.5 Ma, LO 20.6 Ma, Coenen et al. 2025) are reported from 116.5 to 123.8 m (CTZ-61 to CTZ-63).

Cestodiscus is present throughout the CTZ-section, showing the typical succession of species that occurs around the Eocene-Oligocene boundary. *Cestodiscus* aff. *intersectus* (Fig. 4.8) is consistently present from the base up to 116.5 m (CTZ-61), ranging from very rare to common, then scattered and very rare. *Cestodiscus fennerae* (FO 36.9 Ma, LO 35.0 Ma, Barron et al. 2015) (Fig. 4.2) and *Cestodiscus* sp. 2 *sensu* Fenner (FO 33.9 Ma, LO 33.3 Ma, Barron et al. 2015) appear in the assemblages at 51.5 m (CTZ-14). *Cestodiscus fennerae* is very rare to few and disappears around 110.0 m (CTZ-57), while *Cestodiscus* sp. 2 *sensu* Fenner (Fig. 4.6) is very rare and sporadic and is documented only up to sample CTZ-52 (102.5 m). *Cestodiscus convexus* (Fig. 4.4; FO 34.4 Ma Barron et al. 2015, LO 31.2 Ma, Lazarus et al. 2014) ranges from very rare to common. We tentatively mark its first occurrence along the section around 83.0 m (sample CTZ-38). *Cestodiscus trochus* (FO 34.1 Ma, LO 20.6 Ma, Coenen et al. 2025) (Fig. 4.7) first appears at 113.0 m (CTZ-59) and is documented until the top of the section, ranging in abundance from very rare to few. We documented the presence of the early Oligocene species *Cestodiscus robustus* (FO 33.7 Ma, Barron et al. 2015, LO 30.9 Ma, Lazarus et al. 2014) (Fig. 4.5) from sample 138.8 m (CTZ24-D6) up to the top of the section, ranging from very rare to rare in abundance. The early Oligocene *Cestodiscus reticulatus* (FO 33.4 Ma, LO 32.5 Ma, Lazarus et al. 2014) (Fig. 4.3) is very rare and has been only documented in two samples from the uppermost part of the studied section (CTZ-104 and CTZ24-D33, respectively 168.0 and 180.1 m).

The Oligocene genus *Thalassionema* (FO 31.2 Ma, Lazarus et al. 2014) first appears along the section at 144.9 m (CTZ24-D10), becoming a common component of the Oligocene assemblage. Finally, the Oligocene species *Rouxia obesa* (FO 31.2 Ma, Lazarus et al. 2014; Fig. 6.5) is first observed along the section at 144.9 m (CTZ24-D10), ranging from very rare to few in abundance.

4.1.3 Silicoflagellates

Silicoflagellates range from very rare to few along the section. The most representative species documented are, in order of abundance, *Corbisema triacantha* s.l. (Fig. 6.6), *Naviculopsis biapiculata* (Fig. 6.11), *Naviculopsis foliacea* (Fig. 6.12), *Naviculopsis constricta* (Fig. 6.13), *Bachmannocena apiculata* (Fig. 6.8), *Distephanopsis crux* (Fig. 6.10), *Dictyocha aspera*, *Dictyocha deflandrei* and *Corbisema bimucronata*. Rare *Dictyocha hexacantha* were encountered in a few samples (Table S1).

4.1.4 Radiometric dating

The volcanic ash layer CTZ-T88 displays a unimodal and poorly sorted distribution (Fig. 5a), with values falling within the very fine sand to coarse silt fraction

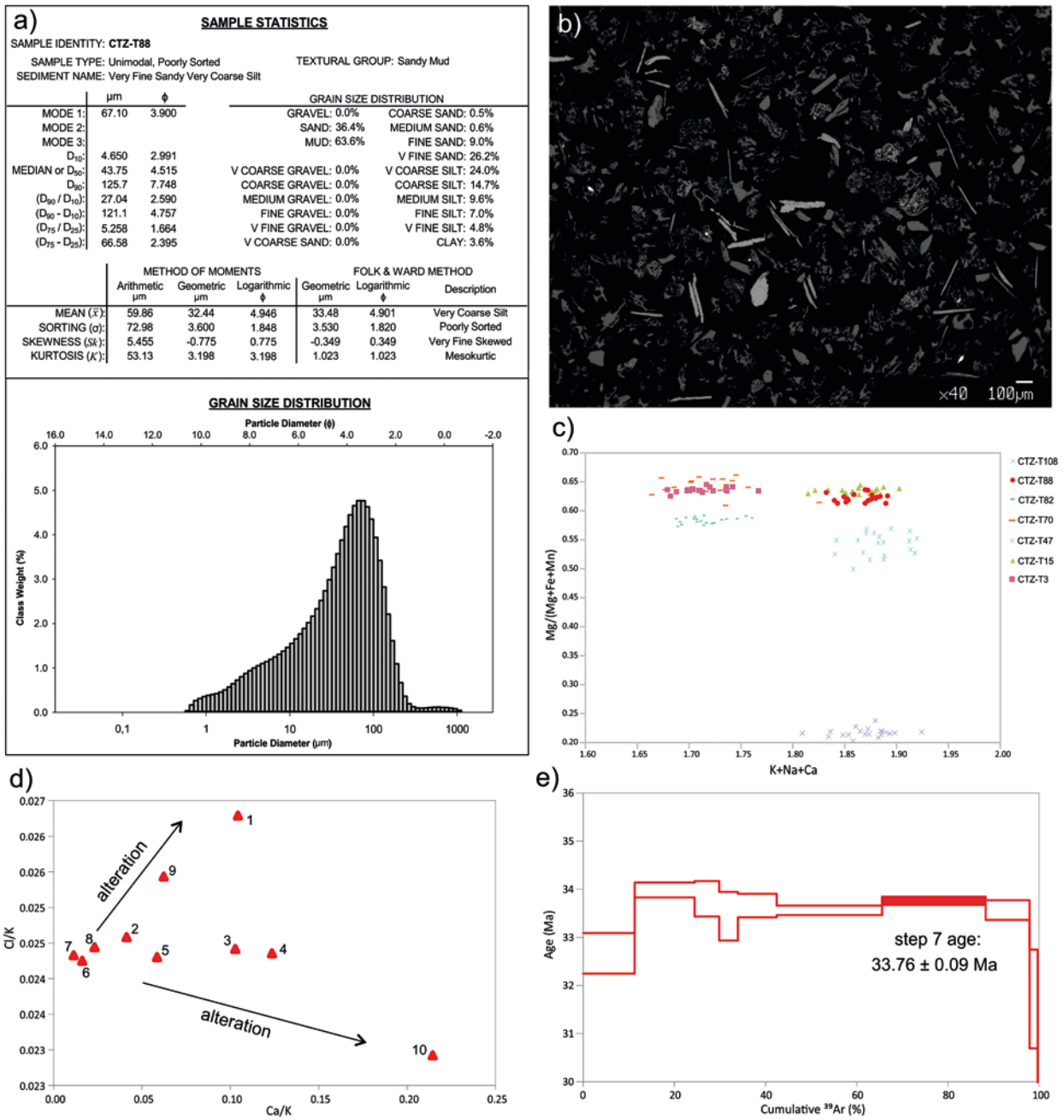

Fig. 5. Characterization of the dated volcanic ash layer CTZ-T88. **a)** Grain-size characterization, obtained with the Grain Size Analysis Program GRADISTAT23 (Blott & Pye 2001) and grain-size distribution curve. Particle diameter is shown as both micrometers (μm) and phi (φ). **b)** BSE image of the 125- to 250-μm-size fraction showing highly vesiculated glass shards (dark grey) and biotite phenocrysts (light grey). **c)** Biotite Mg/(Mg+Fe+Mn) v. K+Na+Ca diagram showing the biotite composition of the analyzed tephra in comparison with the other tephra layers collected along the same stratigraphic log. To obtain statistically significant results, the EPMA analyses were performed on 10 biotite crystals (both rim and core). **d)** Ca/K v. Cl/K diagram showing different patterns of alteration. Ca/K is calculated from the irradiation-produced $^{37}Ar/^{39}Ar$ ratio, Cl/K is calculated from the irradiation-produced $^{38}Ar/^{39}Ar$ ratio. **e)** Age spectrum of the dated tephra. The filled rectangle highlights step 7, i.e., the step that better approximates the Ar release from the unreacted biotite, with the lowest Ca/K.

(Blott & Pye 2001), consistent with primary deposition from distal fallout (Lowe 2011; Griggs et al. 2014). Petrographic observations of the 125–250 µm size fraction (Fig. 5b) show abundant, highly vesiculated glass shards together with fresh biotite phenocrysts and few feldspar and quartz phenocrysts, indicating a primary airfall (Griggs et al. 2014). Electron microprobe analyses of biotite (Fig. 5c) reveal a chemically homogeneous population, with Mg/(Mg+Fe+Mn) values clustering within a narrow range and alkali contents close to stoichiometric values, i.e., 2 apfu (atoms per formula unit), ranging from 1.83 to 1.89 apfu. However, the irradiation-derived K is about 7.37%, below the stoichiometric value of 8%, suggesting a slight alteration in the marine environment (Villa & Bosio 2023). In addition, Ca/K and Cl/K ratios (Fig. 5d) point to the presence of two mineralogical components: a low-Ca/K population corresponding to unaltered biotite, and a high-Ca/K component likely reflecting alteration of a Ca-rich phase, plausibly plagioclase. For the ^{39}Ar–^{40}Ar dating, only the step with the lowest Ca/K, i.e., step 7, was considered to best approximate the argon released from unreacted biotite. The resulting age spectrum (Fig. 5e) identifies step 7 as the most reliable, yielding an age of 33.76 ± 0.09 Ma (2σ), which we interpret as the eruption age of the CTZ-T88 tephra. All the results are reported in Table S2.

4.2 LUN-Section

The LUN-section (Fig. 2) spans the top of the Paracas Formation and the whole Otuma Formation. It consists of 71.5 m of greyish to white-weathered silt, with two tephra layers, a few dolomite layers and one chert-rich interval. The base of the Otuma Formation is represented by 1.5 m of fine sandstone, often forming spherical, meter-sized concretions.

Calcareous nannofossils vary from very rare to common, being particularly abundant in the lower and middle parts of the section, from 4.7 to 38.5 m (MLU-D7 to LUN2-D54) but they are absent from the uppermost layers. Diatoms are generally abundant throughout the section, with a noticeable increase in diversity in the upper part, from 35.5 to 71.5 m (LUN2-D52 to LUN2-D76), exhibiting a trend opposite to that of calcareous nannofossils. Silicoflagellate abundance is scattered and discontinuous. This group is nearly absent in the lower part up to 14.5 m (MLU-D6 to LUN2-D38) and exhibits only rare occurrences in the middle and upper parts of the section. Finally, the species incertae sedis *Macrora stella* is documented in a few samples (Table S1).

4.2.1 Calcareous nannofossils

The calcareous nannofossil assemblages at the LUN-section are characterized, in order of abundance, by *Reticulofenestra, Coccolithus, Isthmolithus, Discoaster, Helicosphaera, Sphenolithus, Zygrhablithus, Pontosphaera, Micrantholithus, Chiasmolithus, Coronocyclus*, and *Blackites*.

Among the stratigraphic markers, *R. umbilicus* exhibits a continuous presence along the LUN-section from 4.7 to 38.5 m (MLU-D7 to LUN2-D54), ranging in abundance from very rare to few. Its last occurrence (LO at 32.02 Ma, Agnini et al. 2014) is documented at 38.5 m (sample LUN2-D54) but is followed by several barren samples. *C. formosus* (LO 32.92, Agnini et al. 2014), although with very rare to rare abundance, is still present up to the top of the section, making the LO of *R. umbilicus* unreliable. *Reticulofenestra reticulata* (Fig. 6.17) is very rare to common and only occurs up to 14.5 m (LUN2-D38), where we define its last occurrence (LO 35.2 Ma, Agnini et al. 2014). *Reticulofenestra isabellae* (Fig. 6.18) is very rare and has been found only in one sample (LUN2-D37), pointing to a Priabonian age (FO 36.70, LO 35.00 Ma). The last occurrence of *Discoaster saipanensis* (Fig. 6.15) is observed at 25.0 m (LUN2-D45), marking the base of the EOT. *Helicosphaera clarissima* (LO 35.71 ± 1.27 Ma) is present from the base of the section with a very rare to rare abundance; its last occurrence is observed at

Fig. 6. Diatoms, silicoflagellates, and calcareous nannofossils the Otuma Formation: 1, 2) *Pyxilla reticulata* (1, CTZ-24; 2, CTZ-58); 3) *Pyxilla reticulata* (variety corresponding to *P. johnsoniana* Forti) (CTZ-27); 4) *Rouxia granda* (LUN2-D63); 5) *Rouxia obesa* (LUN2-D66); 6) *Corbisema triacanta* s.l. (CTZ-98); 7) *Dictyocha deflandrei* (LUN2-D71); 8) *Bachmannocena apiculata* (CTZ-116); 9) *Dictyocha deflandrei*, medusoid form (LUN2-D70); 10) *Distephanopsis crux* (CTZ-98); 11) *Naviculopsis biapiculata* (CTZ-22); 12) *Naviculopsis constricta* (CTZ-38); 13) *Naviculopsis foliacea* (CTZ-32); 14) *Chiasmolithus oamaruensis* (CTZ-23); 15) *Discoaster saipanensis* (LUN2-D43); 16) *Isthmolithus recurvus* (CTZ-98); 17) *Reticulofenestra reticulata* (LUN2-D38); 18) *Reticulofenestra isabellae* (LUN2-D38). Scale bar = 10 µm for all images.

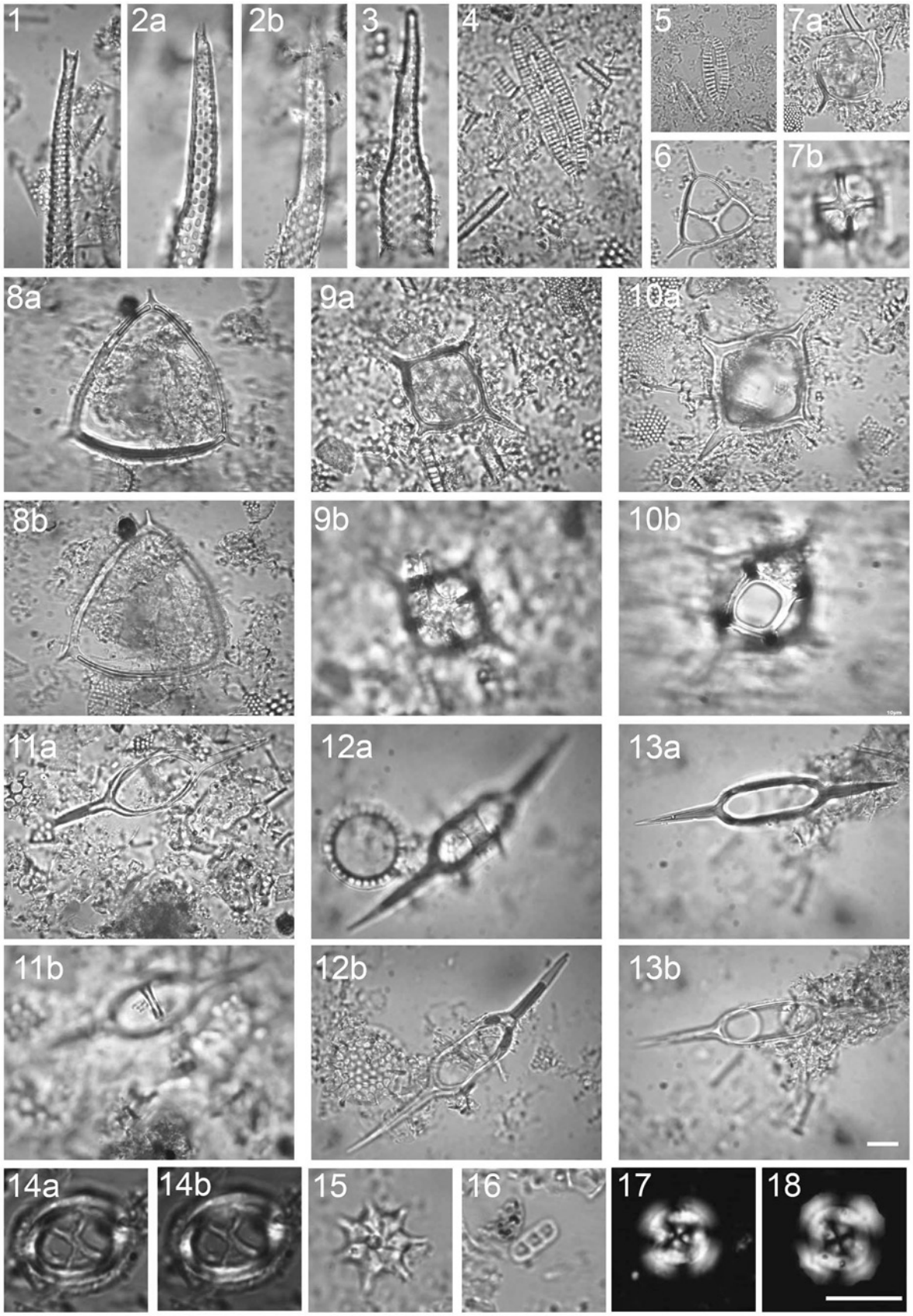
1
2a
2b
3
4
5
7a
6
7b
8a
9a
10a
8b
9b
10b
11a
12a
13a
11b
12b
13b
14a
14b
15
16
17
18

29.5 m (LUN2-D48). *Isthmolithus recurvus* (FO 36.8 Ma, LO 32.47 ± 0.45 Ma) is very rare in our samples, being documented in one sample at the base of the section, then from 7.8 m (LUN2-D8) up to 38.5 m (LUN2-D54). However, its last occurrence is followed by an interval of barren samples. Finally, *Chiasmolithus oamaruensis* (Fig. 6.14), a late Eocene – early Oligocene marker (FO 37.84 Ma, LO 32.02 Ma), is very rare and has been documented only in a few samples.

4.2.2 Diatoms

The LUN-section is characterized by a diverse diatom assemblage which includes, in order of abundance, *Rhizosolenia*, *Stephanopyxis* (Fig. 4.13), *Cestodiscus*, *Coscinodiscus*, *Melosira*, *Paralia*, *Azpeitia*, *Hemiaulus*, *Pyxilla*, *Actinoptychus*, *Thalassionema*, *Rouxia*, *Actinocyclus*, *Triceratium*, *Sceptroneis*, *Rhaphoneis*, and *Arachnoidiscus*. *Chaetoceros* resting spores are very rare to few and have been documented throughout the study interval.

Rhizosolenia spp. is very rare to rare in the lower part of the study interval up to sample 34.0 m (LUN2-D51). Beyond this point, its abundance increases, ranging from few to common. The *Cestodiscus* genus at the LUN-section exhibits lower diversity and abundance compared to the CTZ-section. *Cestodiscus* aff. *intersectus* (late Eocene to Miocene, Strelnikova et al. 2001; Fig. 4.8) is very rare to few, yet it appears in most of the analyzed samples. *Cestodiscus trochus* (FO 34.1 Ma, LO 20.6 Ma, Coenen et al. 2025) (Fig. 4.7) and *Cestodiscus convexus* (FO 34.4 Ma, Barron et al. 2015, LO 31.2 Ma, Lazarus et al. 2014; Fig. 4.4) are very rare to rare, and appear at 31.0 m (LUN2-D49) and 26.5 m (LUN2-D46), respectively. *Cestodiscus robustus* (FO 33.7 Ma, Barron et al. 2015, LO 30.9 Ma, Lazarus et al. 2014) was not found along this section. However, we identified very rare specimens of a form that we tabulated as *Cestodiscus* cf. *robustus* in the upper part of the study interval, starting from sample LUN2-D59 (46.0 m, Table S1).

Hemiaulus is very rare to rare and mostly represented by the middle Eocene to early Oligocene *H. polycystinorum* (Fenner 1978; Fig. 4.10), and by the late Paleocene to early Oligocene *Hemiaulus subacutus* (FO 57.1 Ma, Barron et al. 2015, LO 30.1 Ma, Lazarus et al. 2014) (Fig. 4.11). Both species are present from the base of the interval; *H. polycystinorum* has been documented until the top of the interval (71.5 m), while *H. subacutus* disappears around 49.0 m (LUN2-D61). Very rare specimens of *H. subacutus* with basal constrictions (Fig. 4.12), a typical marker of the early Oligocene (Fenner 1985), have been documented in a few samples from the upper part of the interval, above 40.0 m.

Pyxilla is few to common in the lowermost part of the section, up to 41.5 m, then its abundance upwards is very rare and scattered. It is represented by the middle Eocene to early Oligocene *Pyxilla reticulata* (FO 46.6, Barron et al. 2015, LO 30.9 Ma, Lazarus et al. 2014) (Fig. 6.1, 6.2). *Azpeitia* is consistently present throughout the section, with abundance ranging from very rare to few. It includes *Azpeitia tuberculata/oligocenica*, a transitional form that typically occurs at the end of the late Eocene (FO 37 Ma, LO 33.9 Ma, Barron et al. 2014), and rare *Azpeitia* cf. *oligocenica*. *Thalassionema*, a genus that appeared 31.2 Ma, first appears at 35.5 m (LUN2-D52) and is very rare to rare in abundance. The Oligocene species *Rouxia obesa* (FO 31.2 Ma, LO 21.3 Ma, Lazarus et al. 2014; Fig. 6.5) first appears at 46.0 m (LUN2-D59) and ranges from few to abundant. We also identified a few specimens of *Rouxia granda* (Fig. 6.4), whose FO is the latest Eocene (FO 34.7 Ma, Barron et al. 2015, LO 29.5 Ma, Lazarus et al. 2014).

4.2.3 Silicoflagellates

Silicoflagellates are represented by very rare specimens of *Corbisema triacantha* s.l. (Fig. 6.6), followed, in order of abundance, by *Naviculopsis foliacea* (Fig. 6.13), *Naviculopsis biapiculata* (Fig. 6.11), *Distephanopsis crux* (Fig. 6.10), *Naviculopsis constricta* (Fig. 6.12), *Bachmannocena apiculata* (Fig. 6.8), and *Dictyocha deflandrei* (Fig. 6.7). All silicoflagellates are typical late Eocene species that continue in the Oligocene and in particular *D. deflandrei*, which also occurs with a medusoid specimen (Fig. 6.9), is documented close to the Eocene–Oligocene transition.

5. Discussion

5.1 Chronostratigraphy

Few previous studies of the Paleogene record of the EPB have focused on the Eocene strata, and comprehensive biostratigraphic analyses remain scarce (Fourtanier & Macharé 1988; Marty et al. 1988; DeVries et al. 2006, 2017; Lambert et al. 2017, 2019; Coletti et al. 2019, 2026; DeVries 2019; de Muizon et al. 2019; Collareta et al. 2020; Malinverno et al. 2021).

Although the presence of Oligocene strata has been pointed out by DeVries et al. (2017), detailed studies focusing on the Oligocene deposits in the basin were hitherto lacking, leaving a significant gap in understanding the Eocene–Oligocene transition in this area. Therefore, the present study fills this gap by developing a high-resolution biostratigraphic framework of the Otuma Formation at two locations in the EPB, integrating calcareous nannofossil, diatom, and silicoflagellate biostratigraphy. The early Oligocene is not only a crucial paleoclimatic interval, but in the EPB it marks the transition to an uplift phase of the forearc, following the Eocene extensional tectonic regime (DeVries 1998; Di Celma et al. 2022).

The record of calcareous nannofossils is discontinuous along both sections; abundances decrease upwards, with the uppermost samples being barren. In both sections, the assemblages are characterized by low diversity and are dominated by robust placoliths, such as *R. bisecta*, *R. dictyoda*, and *R. umbilicus*. A similar dominance has been documented in other upper Eocene sections of the EPB (Lambert et al. 2017; Malinverno et al. 2021) and suggests a depleted assemblage. Many key stratigraphic markers from the late Eocene to early Oligocene identified by Agnini et al. (2014) are either absent or very rare, which could be related to species-specific environmental preferences, strong dilution by biogenic opal/terrigenous material, or selective postdepositional dissolution. For example, *Clausicoccus subdistichus*, whose first common occurrence (or Base common) is a well-established bioevent marking the Eocene–Oligocene boundary (Viganò et al. 2023), is notably absent throughout the analyzed sediment section. Although this species has been predominantly recorded in deep-water settings (e.g., Agnini et al. 2014; Marino & Flores, 2002; Toffanin et al. 2013; Viganò et al. 2023), several authors report it also from shallow water successions (Bown 2005; Dunkley Jones et al. 2008; Shepherd & Kulhanek 2016; Jones & Dunkley Jones 2020; Messaoud et al. 2020; Kaya et al. 2025), so that it is unlikely that its absence in the EPB can be simply explained due to proximity to the coast. Recently, the increase in abundance (and size) of this species at the Eocene–Oligocene boundary has been explained as a response to increased nutrient availability and ocean alkalinity occurring at this transition (Viganò & Agnini 2025). Although nutrient concentrations likely increased also in the EPB, other environmental factors might have limited the growth of this species, or its signal was deleted by selective dissolution.

Nevertheless, we identified several valuable calcareous nannofossil bioevents that provide a basis for correlating the sections and are used as tie points for the age model.

The lower part of both sections is characterized by the presence of typical late Priabonian marker species. *Isthmolithus recurvus* is present from the basal portion of the CTZ section and its first occurrence (36.8 Ma) is identified just above the base of the LUN section. This species is typically observed during a brief interval around 37.2 Ma, known as the *I. recurvus* spike, before disappearing and re-emerging at 36.8 Ma where its first occurrence is defined (Agnini et al. 2014; Fornaciari et al. 2010). This spike may account for the presence of one single specimen of *I. recurvus* observed at the top of the Paracas Formation at LUN.

Reticulofenestra reticulata ranges from very rare to common and its last occurrence (35.24 Ma, Agnini et al. 2014) is identified in the lower part of the CTZ-section (81.5 m, CTZ-37) and LUN-section (14.5 m, LUN2-D38).

The last occurrence of *D. saipanensis* (34.44 Ma, Agnini et al. 2014) is recorded a few meters above (106.25 and 25.75 m at CTZ and LUN, respectively). Although the rare and sporadic presence of this species and the occurrence of barren samples undermines its reliability as a biostratigraphic marker here, its presence defines a minimum age and is therefore used (with large vertical error bars) while building the age model.

Helicosphaera clarissima is not used as a chronostratigraphic marker in biozonal schemes, as its last occurrence is globally diachronous (LO 35.71 ± 1.27 Ma, Young et al. 2024). However, its last occurrence, placed between the last occurrence of *R. reticulata* (35.24 Ma) and the last occurrence of *D. saipanensis* (34.44 Ma) along the two sections, provides a useful marker for local correlations.

Both sections contain typical late Eocene diatom marker species, in particular those related to the genus *Cestodiscus*. Several species of this genus are characterized by short and well-defined stratigraphic ranges in the middle Eocene to early Oligocene interval (Barron et al. 2015; Lazarus et al. 2014; Strelnikova et al. 2001). In our samples, the highest diversity of *Cestodiscus* has been documented at the CTZ-section, while at the LUN-section this genus displays a lower abundance and diversity, so that some important markers were not recorded (e.g., *C. fennerae* and *C. robustus*).

Cestodiscus fennerae (36.9–35.0 Ma) defines the *C. fennerae* Biozone (Barron et al. 2015). The pres-

ence of this species in the lower portion of the studied CTZ-section supports a late Priabonian age for this interval. Its LO is identified at 110.0 m (CTZ22-57) and used as a tie point in the age model. No specimens of *C. fennerae* have been observed at the LUN-section, probably due to the overall low abundance of diatoms here.

The transition to the Oligocene is marked by several bioevents. The first occurrence of *C. robustus* (FO 33.7 Ma), which defines the *C. robustus* Biozone (Barron et al. 2015), is documented only at CTZ. At LUN, due to the lower abundance and diversity of the *Cestodiscus* genus, no specimens of *C. robustus* were observed. The first occurrence of the genus *Thalassionema* (FO 31.2 Ma), and the first occurrence of the Oligocene species *Rouxia obesa* (FO 31.2 Ma; Lazarus et al. 2014) were observed at both sections. The latter was in fact previously observed from only one sample at Cerro Tiza (DeVries et al. 2017). Some uncertainty regarding the age of first appearance of *R. obesa* arises from discrepancies in the literature: Lazarus et al. (2014) report its first occurrence at 31.2 Ma, whereas DeVries et al. (2017) suggest an age of 33.8 Ma for the same event. In our work, the absolute dating of tephra CTZ-T88 at 33.76 ± 0.09 Ma, a few meters above the identified FO of both *T. nitzschioides* and *R. obesa* supports the findings of DeVries et al. (2017) and thus suggests an older first occurrence of both taxa.

The last occurrences of calcareous nannofossil *Coccolithus formosus* (LO 32.92 Ma), *I. recurvus* (LO 32.47 ± 0.45 Ma) and *R. umbilicus* (LO 32.02 Ma) take place sequentially along the Rupelian. These events cannot be defined at CTZ because of the absence of nannofossils in the corresponding samples. At LUN, this interval coincides with a significant drop in calcareous nannofossil abundance and several barren samples, so these bioevents must be considered with caution here and are not used as tie points in the age model.

The sparse silicoflagellates support a latest Eocene to early Oligocene age. In both sections, we identified sparse specimens of the late Eocene–early Oligocene *D. deflandrei* (Perch-Nielsen, 1985b), the Eocene species *N. foliacea* and *N. constricta* (McCartney et al. 2020) as well as *N. biapiculata*, which appeared in the late Eocene, becoming the dominant *Naviculopsis* species in the early Oligocene. As we move higher in the sections, a shift in abundance between *N. foliacea* and N. *biapiculata* is observed (Table S1), even though the number of specimens considered here is not statistically significant. Finally, rare *D. hexacantha*, defining the *D. hexacantha* zone (36.6–34.6 Ma, Barron et al. 2014) were only recovered from the basal part of the section, supporting the latest Eocene age inferred for this interval.

5.2 Age model and sedimentation rates

The age-depth models for the CTZ and LUN sections (Fig. 7) were developed using the biostratigraphic data and the absolute dating of CTZ-T88 as tie points. Table 1 summarizes all the bioevents that characterize this interval, the stratigraphic position at which they were identified at CTZ and LUN and their reliability for the two studied sections. Both sections span the upper Eocene (Priabonian, 37.71–33.90 Ma) to lower Oligocene (Rupelian, 33.90–27.30 Ma), and are bounded at the bottom by the presence (at CTZ) or first occurrence (at LUN) of *I. recurvus* (FO 36.84 Ma).

The lower number of bioevents at LUN is due to the lower abundance of diatoms, resulting in a lower abundance and diversity of *Cestodiscus* at this locality. The only silicoflagellate bioevent for this interval (LO of *D. hexacantha*) cannot be used, due to the scattered presence of the marker species and of silicoflagellates in general. Nevertheless, silicoflagellates provide supporting evidence for the Priabonian–Rupelian age of the section (e.g., the presence of the marker species *D. hexacantha* in the basal CTZ samples and the shift in relative abundance from the Eocene *N. foliacea* to the late Eocene to early Oligocene *N. biapiculata*).

The average linear sedimentation rates calculated from the age model for the two study sections is 75.5 m/My at CTZ and 8.1 m/My at LUN. The markedly different sedimentation rates characterizing the two depocenters is interpreted as resulting from variable amounts of sediment input: this was significantly more abundant for the more proximal and restricted CTZ depocenter than for the more distal, open marine, small LUN depocenter (Fig. 8). Because no significant apparent change in the proportion of biogenic and lithogenic particles is observed between the two sites, it is likely that changes in the amount of lithogenic material also impacted on biogenic productivity (but a quantitative estimate through e.g. XRF analyses is recommended).

Following Hutchinsons et al. (2021), the stratigraphic position of the EOT is constrained between the LO of *D. saipanensis* (34.44 Ma) and the "earliest Oligocene oxygen isotope step" (EOIS, 33.65 Ma), the latter corresponding with the Oi1-event of Miller et al.

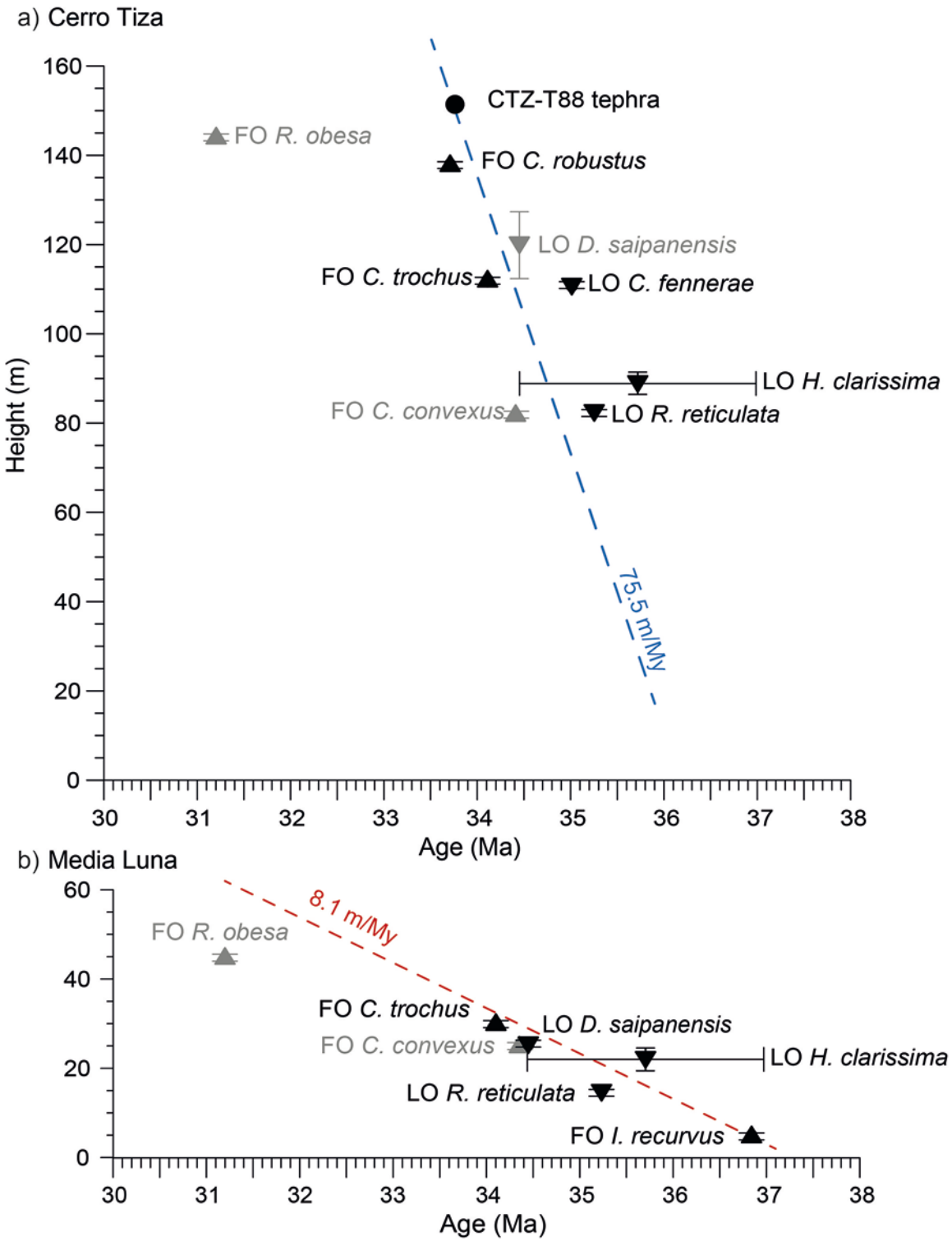

Fig. 7. Age models for the Otuma Formation based on diatom and calcareous nannofossil bioevents (from Table 1) for the two localities: **a)** Cerro Tiza; **b)** Media Luna. The age of CTZ-T88 was also used as a tie point at Cerro Tiza.

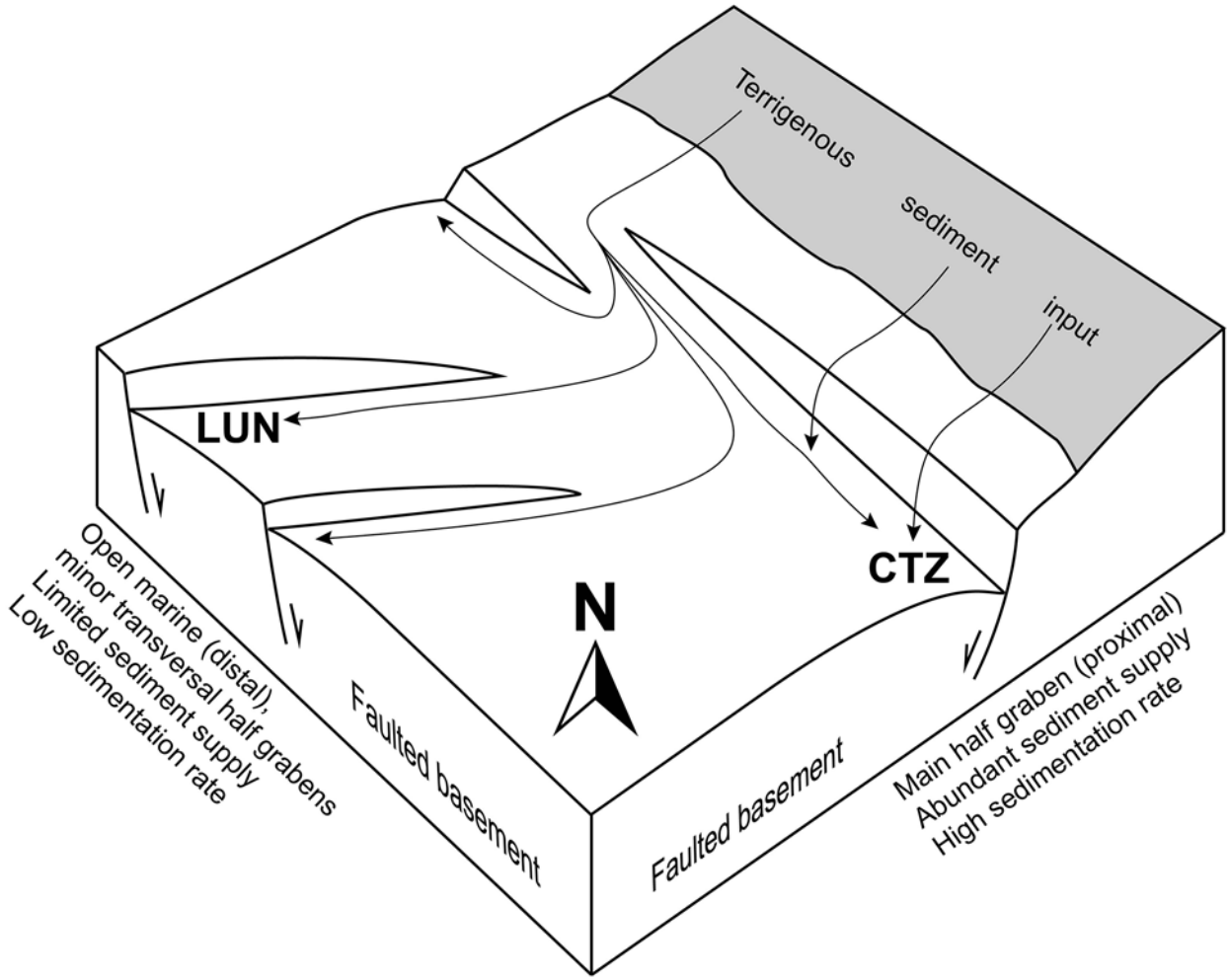

Fig. 8. 3D cartoon showing the schematic location of the Cerro Tiza (CTZ) and Media Luna (LUN) stratigraphic successions within the half-grabens (location in Fig. 1b).

(1991) and the Oi-1a event of Zachos et al. (1996). Although an unambiguous identification of the EOT relies on a stable oxygen isotope record, the low carbonate content of CTZ and LUN successions (< 5% in samples containing calcareous nannofossils, Regattieri pers. comm.) prevented this analysis. Therefore, while the base of the EOT is placed in correspondence with the LO of *D. saipanensis*, the top of the event is not well constrained. The stratigraphic position of the Eocene–Oligocene boundary (33.9 Ma) was calculated from the age models, assuming a constant sedimentation rate between consecutive tie points, and is located at 136 m at CTZ and 31 m at LUN.

5.3 Paleoecological perspectives

The Otuma Formation at Cerro Tiza and Media Luna provides a record of the Eocene–Oligocene boundary and of the EOT, one of the most critical climatic transitions of the Cenozoic (Coxall & Pearson 2007; Hutchinson et al. 2021). At the global scale, the EOT marks the shift from the warmhouse climate of the Eocene to the coolhouse conditions of the Oligocene, and is characterized by a sharp global cooling, the first large-scale glaciation of Antarctica, a drop in global sea surface temperatures, and a reorganization of the deep ocean circulation (Miller et al. 1991; Diester-Haass & Zachos 2003; Pälike et al. 2006; Coxall & Wilson 2011; Zachos et al. 2008; Sun et al. 2014; Westerhold et al. 2020; Hutchinson et al. 2021; Śliwińska et al. 2023). It also involves a major pertur-

bation of the global carbon cycle with a general decline in atmospheric CO_2 levels, the sudden and permanent deepening of the carbonate compensation depth (CCD), and an increase in deep water $\delta^{13}C$ values (Coxall & Pearson 2007; Coxall et al. 2005; Hutchinson et al. 2021; Miller et al. 2009).

In the world oceans, the EOT is characterized by cooling and an increase in productivity, testified by an overall decrease of calcareous nannofossil abundance and diversity (Bown et al. 2004; Dunkley Jones et al. 2008; Jones et al. 2019; Nyerges et al. 2021; Viganò et al. 2024), an increase in the abundance and size of small calcareous nannofossils (Viganò & Agnini, 2025) and a significant increase of the abundance and diversity of diatoms, which led to their current ecological dominance (Cervato & Burckle 2003; D'haenens et al. 2014; Egan et al. 2013; Lazarus et al. 2014; Renaudie 2016; Suto et al. 2012; Bryłka et al. 2024) due to their ability to thrive during glacial periods (Iglesias-Rodríguez et al. 2002; Tozzi et al. 2004).

In the EPB, calcareous nannofossils show a shift in dominance from warm-water taxa (*C. formosus*, *C. eopelagicus*, and *C. pelagicus*) to cool-water taxa (*R. reticulata* and large *Reticulofenestra*) at the top of the Paracas Formation around 38 Ma (Malinverno et al. 2021; Bianucci et al. 2023). Throughout the Otuma Formation, they display low diversity assemblages dominated by large *Reticulofenestra* (Malinverno et al. 2021 and this work), typical of temperate-cool waters and mesotrophic-eutrophic environments (Persico & Villa 2004; Villa et al. 2008, 2014; Wade & Bown 2006) and disappear just before (at CTZ the LO of *D. saipanensis* occurs within 30 m of barren samples followed by the sporadic occurrence of nannofossils above) or within the EOT (at LUN, calcareous nannofossils disappear after the LO of *D. saipanensis*).

The disappearance of calcareous nannofossils around the EOT is uncommon and might be due to ecological or post-depositional factors. Deep-sea records testify a transition from non-calcareous to calcareous-dominated sediments in correspondence with the CCD deepening associated with the EOT (Coxall et al. 2005; Pälike et al. 2012; Taylor et al. 2023; Wade et al. 2020), making dissolution an unlikely explanation. However, the increase in productivity resulting from the strengthening of the Humboldt Current upwelling system could have caused a shallowing of the CCD in the oxygen minimum zone, similar to recent conditions with the CCD at shelf depths on the Peruvian margin (e.g. Suess et al. 1988). In alternative, elevated productivity and fast organic matter burial could have promoted supralysoclinal carbonate dissolution, a process that occurs in shallow marine environments (Adler et al. 2001; Peterson & Prell 1985), due to microbial activity that increases pore-water CO_2 (Archer et al. 1989; Baker 2016; Jahnke et al. 1994; Schulte & Bard 2003; Wenzhöfer et al. 2001).

Diatoms are not present in the Paracas Formation and the lower portions of the Otuma Formation but occur well above the FO of *I. recurvus*, since ~ 36 Ma (Malinverno et al. 2021). Upper Eocene diatom assemblages from previously studied EPB sections, as well as in this work, are characterized by high abundances of *Rhizosolenia*, *Stephanopyxis*, *Hemiaulus*, *Pyxilla*, and large *Coscinodiscus*. These genera are typically associated with stratified water conditions (Davies & Kemp 2016; Davies et al. 2009; McKay et al. 2000) and a deep chlorophyll maximum (Kemp et al. 2000), indicating a seasonal rather than year-round increase in nutrients (Malinverno et al. 2021). Even if *Rhizosolenia* is associated with highly productive waters of the equatorial Pacific (Benton & Pearson 2001), its trophic strategy relies on vertical migration to feed at the nutricline and/or on the symbiotic relationship with diazotrophic cyanobacteria, making it part of the "shade flora" (Kemp et al. 2000) of stratified ocean settings. *Chaetoceros* resting spores, indicative of high nutrient concentrations, are present throughout the succession with limited abundances, but display a slight increase in the early Oligocene, where also the high-productivity genus *Thalassionema* appears, together with other thinly-silicified genera of the Eocene to Miocene diatom turnover (Baldauf 1992). *Cestodiscus* displays an increase in abundance during the latest Eocene and along the EOT, along with its global species radiation. Although the ecological preferences of *Cestodiscus* are unclear, the global increase in abundance and diversity of this genus in the latest Eocene–early Oligocene, in particular in the Southern Ocean (e.g. Özen et al. 2026) suggests an overall preference for cool waters and high trophic levels.

Overall, the calcareous nannofossil and diatom record in the EPB document the cooling trend that began in the late Priabonian and culminated in the EOT and indicate increased nutrient availability in the basin, although never reaching permanently eutrophic conditions.

The difference in phytoplankton assemblages along the two investigated sections could be explained by the different paleoenvironmental setting witnessed by the two locations. CTZ represents a depocentral area of the EPB, located on the continental shelf. The

presence of taxa such as calcareous nannofossils of nearshore environments (e.g. *Micrantholithus* sp. and *Z. bijugatus*) and benthic and/or coastal diatoms (e.g. *Actinoptychus* sp., *Paralia* sp., *Stephanopyxis* sp., raphid pennate diatoms), and abundant lithogenic material points to a setting not far from the shore, characterized by a high (75.5 m/My) sedimentation rate. However, because the depositional setting was not affected by the sea-level drop associated with the EOT (60–80 m, Hutchinsons et al. 2021), the paleodepth was likely between 100 and 200 m. The presence of laminated diatomites, fish debris, and plant remains support a low energy environment. The LUN section represents the sediment filling of a small half-graben basin (Fig. 8). Although it likely attained a similar depositional depth (i.e., similar concentrations of nearshore taxa) as CTZ, due to its position in a more distal position, LUN received a limited sediment supply, leading to reduced sedimentation rates (8.1 m/My).

6. Conclusions and future perspectives

We developed a biostratigraphic framework by integrating calcareous nannofossil, diatom, and silicoflagellate data along the stratigraphic sections of Cerro Tiza and Media Luna in the Otuma Formation. Though discontinuous and characterized by low diversity, the calcareous nannofossil record reveals assemblages dominated by large placoliths such as *Reticulofenestra bisecta*, *R. dictyoda*, and *R. umbilicus*. Although some important early Oligocene markers like *Clausicoccus subdistichus* are absent, other valuable bioevents like the FO of *Isthmolithus recurvus* (FO at 36.8 Ma), the LO of *Reticulofenestra reticulata* (LO at 35.24 Ma), and the LO of *Discoaster saipanensis* (LO at 34.44 Ma) provide a robust chronologic framework for the late Priabonian. Among diatoms, the succession of species of genus *Cestodiscus* provide key biostratigraphic information at CTZ but not at LUN, where overall diatom abundance is low and this genus is rare. The FO of *Rouxia obesa* and *Thalasionema nitzschioides* are documented at CTZ in the earliest Oligocene, well before their known range, as supported by the CTZ-T88 tephra layer dated at 33.76 Ma, occurring just below the layer at which their first occurrence was detected. Silicoflagellates, including species such as *Naviculopsis foliacea* and *N. biapiculata*, and the rare occurrence of *Dictyocha hexacantha*, support the chronological framework.

The age models, based on the identified bioevents, allowed to define the position of the Eocene-Oligocene boundary and to calculate the linear sedimentation for the two sections, 75.5 m/My at CTZ and 8.1 m/My at LUN.

A gradual decline in calcareous nannofossils up to their total disappearance around the EOT and an increase in diatoms is qualitatively observed along the two sections. Such change, that parallels that observed in the world oceans, reflects the combined effects of global climatic cooling, regional oceanographic changes, and nutrient dynamics, although local CCD-related or postdepositional dissolution can play a role in the disappearance of calcareous nannofossils. Differences between the CTZ and LUN sections highlight the diverse depositional settings within the basin, with CTZ representing a larger depocenter in a land-proximal setting, characterized by a higher sediment input, and LUN representing a smaller depocenter, more connected to the open ocean.

While stable oxygen isotope records are commonly used to identify the EOT, the low carbonate content of the CTZ and LUN successions (< 5% in samples containing calcareous nannofossils) prevents this analysis. Future studies could benefit from additional geochemical investigations as well as quantitative microfossil work to further constrain paleoceanographic and paleoenvironmental changes across these key sections.

Acknowledgements. We thank Tom J. DeVries for fruitful discussion on the EOT in the Pisco Basin and John Barron for illuminating exchanges on diatoms. A special thanks to Valentina Barberini and Nicoletta Fusi for absolute dating and grain-size analyses. The authors wish to thank also Andrea Risplendente and Stefano Poli for the EPMA analysis, and we mourn the passing of Stefano Poli after the acceptance of this manuscript. WDS analyses were performed at the EPMA facility of the Unitech CO-SPECT at the University of Milan (Italy). The authors also thank Eleonora Regattieri for fruitful discussion on stable isotopes. Financial support for this research was provided by the European Union – Next GenerationEU, Mission 4, Component 2, CUP I53D23002070 006 – Project title: "BIOVERTICES – BIOdiversity of VERTebrates In the CEnozoic Sea" to Alberto Collareta, Elisa Malinverno and Claudio Di Celma, and by the Italian Ministry of University and Research (MUR) through the PRIN 2022 call (ranking list advancement; D.D. 1401/2024) – Project title: "ITAL – Innovations in Thermochronology applied to the Andean natural laboratory" (code 20225Z84SN, CUP J53C24002940006) to Stefano Mazzoli. The authors would like to thank also the two anonymous reviewers and the Editor, for their fruitful comments that improved the paper.

References

Ayala-Carazas, L., Viveen, W., Baby, P., Uribe-Ventura, R., Binnie, S. A., Sanjurjo-Sánchez, J., & Beltrán-Castañon, C. (2026). Quaternary tectonic shortening and uplift of the Peruvian forearc due to subduction of the Nazca Ridge. *Gondwana Research, 153*, 323–343. https://doi.org/10.1016/j.gr.2025.12.008

Adler, M., Hensen, C., Wenzhöfer, F., Pfeifer, K., & Schulz, H. D. (2001). Modeling of calcite dissolution by oxic respiration in supralysoclinal deep-sea sediments. *Marine Geology, 177*(1–2), 167–189. https://doi.org/10.1016/S0025-3227(01)00130-X

Agnini, C., Fornaciari, E., Raffi, I., Catanzariti, R., Pälike, H., Backman, J., & Rio, D. (2014). Biozonation and biochronology of Paleogene calcareous nannofossils from low and middle latitudes. *Newsletters on Stratigraphy, 47*(2), 131–181. https://doi.org/10.1127/0078-0421/2014/0042

Archer, D., Emerson, S., & Reimers, C. (1989). Dissolution of calcite in deep-sea sediments: pH and O2 microelectrode results. *Geochimica et Cosmochimica Acta, 53*(11), 2831–2845. https://doi.org/10.1016/0016-7037(89)90161-0

Baby, P., Prudhomme, A., Brusset, S., Robert, A., Roddaz, M., Calderon, Y., . . . Salas-Gismondi, R. (2025). The Northern Central Andes and Andean tectonic evolution revisited: An integrated stratigraphic and structural model of three superimposed orogens. *Earth-Science Reviews, 260*, 104998. https://doi.org/10.1016/j.earscirev.2024.104998

Baldauf, J. G. (1992). Middle Eocene through early Miocene diatom floral turnover. Eocene-Oligocene climatic and biotic evolution, 310. https://doi.org/10.1515/9781400862924.310

Barron, J., Bukry, D., & Poore, R. Z. (1984). Correlation of the middle Eocene Kellogg Shale of northern California. *Micropaleontology, 30*(2), 138–170. https://doi.org/10.2307/1485715

Barron, J. A., & Baldauf, J. G. (1995). Cenozoic marine diatom biostratigraphy and applications to paleoclimatology and paleoceanography. *Short Courses in Paleontology, 8*, 107–118. https://doi.org/10.1017/S2475263000001446

Barron, J. A., Fourtanier, E., & Bohaty, S. M. (2004). Oligocene and earliest Miocene diatom biostratigraphy of ODP Leg 199 Site 1220, equatorial Pacific. In Proceedings of the Ocean Drilling Program: Scientific Results (Vol. 199).

Barron, J. A., Bukry, D., & Gersonde, R. (2014). Diatom and silicoflagellate biostratigraphy for the late Eocene: ODP 1090 (sub-Antarctic Atlantic). *Nova Hedwigia. Beiheft, 143*, 1–32.

Barron, J. A., Stickley, C. E., & Bukry, D. (2015). Paleoceanographic, and paleoclimatic constraints on the global Eocene diatom and silicoflagellate record. *Palaeogeography, Palaeoclimatology, Palaeoecology, 422*, 85–100. https://doi.org/10.1016/j.palaeo.2015.01.015

Benton, M. J., & Pearson, P. N. (2001). Speciation in the fossil record. *Trends in Ecology & Evolution, 16*(7), 405–411. https://doi.org/10.1016/S0169-5347(01)02149-8

Bianucci, G., & Collareta, A. (2022). An overview of the fossil record of cetaceans from the East Pisco Basin (Peru). *Bollettino della Società Paleontologica Italiana, 61*(1), 19–20.

Bianucci, G., Di Celma, C., Collareta, A., Landini, W., Post, K., Tinelli, C., . . . Malinverno, E. (2016). Fossil marine vertebrates of Cerro Los Quesos: Distribution of cetaceans, seals, crocodiles, seabirds, sharks, and bony fish in a late Miocene locality of the Pisco Basin, Peru. *Journal of Maps, 12*(5), 1037–1046. https://doi.org/10.1080/17445647.2015.1115785

Bianucci, G., Lambert, O., Urbina, M., Merella, M., Collareta, A., Bennion, R., . . . Amson, E. (2023). A heavyweight early whale pushes the boundaries of vertebrate morphology. *Nature, 620*(7975), 824–829. https://doi.org/10.1038/s41586-023-06381-1

Blott, S. J., & Pye, K. (2001). Gradistat: A grain size distribution and statistics package for the analysis of unconsolidated sediments. *Earth Surface Processes and Landforms, 26*(11), 1237–1248. https://doi.org/10.1002/esp.261

Bolli, H. M., Saunders, J. B., & Perch-Nielsen, K. (1989). *Plankton Stratigraphy* (Vol. 2). Radiolaria, Diatoms, Silicoflagellates, Dinoflagellates and Ichthyoliths. CUP Archive.

Bosio, G., Gioncada, A., Malinverno, E., Di Celma, C., Villa, I. M., Cataldi, G., . . . Bianucci, G. (2019). Chemical and petrographic fingerprinting of volcanic ashes as a tool for high-resolution stratigraphy of the upper Miocene Pisco Formation (Peru). *Journal of the Geological Society, 176*(1), 13–28. https://doi.org/10.1144/jgs2018-071

Bosio, G., Gioncada, A., Di Celma, C., Villa, I. M., Pichavant, M., Urbina, M., & Bianucci, G. (2020a). Two-mica rhyolitic tephra in the East Pisco Basin (Peru): New age and dispersion constraints for the eruptions of the Eastern Cordillera of Central Andes. *Bulletin of Volcanology, 82*(6), 1–22. https://doi.org/10.1007/s00445-020-1373-y

Bosio, G., Malinverno, E., Villa, I. M., Di Celma, C., Gariboldi, K., Gioncada, A., . . . Bianucci, G. (2020b). Tephrochronology and chronostratigraphy of the Miocene Chilcatay and Pisco formations (East Pisco Basin, Peru). *Newsletters on Stratigraphy, 53*(2), 213–247. https://doi.org/10.1127/nos/2019/0525

Bosio, G., Collareta, A., Di Celma, C., Lambert, O., Marx, F. G., de Muizon, C., . . . Bianucci, G. (2021). Taphonomy of marine vertebrates of the Pisco Formation (Miocene, Peru): Insights into the origin of an outstanding Fossil-Lagerstätte. *PLoS One, 16*(7), e0254395. https://doi.org/10.1371/journal.pone.0254395

Bosio, G., Gioncada, A., Malinverno, E., Coletti, G., Collareta, A., Mariani, L., . . . Di Celma, C. (2024). Unraveling marine phosphogenesis along the Miocene coast of Peru: Origin and sedimentological significance of the Pisco Formation phosphorites. *Marine and Petroleum*

Geology, 167, 106941. https://doi.org/10.1016/j.marpetgeo.2024.106941

Bown, P. R. (2005). Calcareous nannoplankton evolution: A tale of two oceans. *Micropaleontology, 51*(4), 299–308. https://doi.org/10.2113/gsmicropal.51.4.299

Bown, P. R., & Young, J. R. (1998). Introduction. In P. R. Bown (Ed.), *Calcareous Nannofossil Biostratigraphy, British Micropalaeontology Society Series* (pp. 1–15). London: Chapman & Hall. https://doi.org/10.1007/978-94-011-4902-0_1

Bown, P. R., Lees, J. A., & Young, J. R. (2004). Calcareous nannoplankton evolution and diversity through time. *Coccolithophores: from molecular processes to global impact*, 481–508. https://doi.org/10.1007/978-3-662-06278-4_18

Bryłka, K., Witkowski, J., & Bohaty, S. M. (2024). Biogenic silica accumulation and diatom assemblage variations through the Eocene-Oligocene Transition: A Southern Indian Ocean versus South Atlantic perspective. *Palaeogeography, Palaeoclimatology, Palaeoecology, 636*, 111971. https://doi.org/10.1016/j.palaeo.2023.111971

Bukry, D. (1981). Synthesis of silicoflagellate stratigraphy for Maastrichtian to Quaternary marine sediments. *SEPM Spec. Publ., 32*, 433–444.

Bukry, D. (1987). Eocene siliceous and calcareous phytoplankton, Deep Sea Drilling Project Leg 95. In K. L. Turner (Ed.), *Initial Reports of Deep Sea Drilling Project* (pp. 395–415). U.S. Government Printing Office. https://doi.org/10.2973/dsdp.proc.95.112.1987

Cervato, C., & Burckle, L. (2003). Pattern of first and last appearance in diatoms: Oceanic circulation and the position of polar fronts during the Cenozoic. *Paleoceanography, 18*(2), 2002PA000805. https://doi.org/10.1029/2002PA000805

Clarke, J. A., Ksepka, D. T., Stucchi, M., Urbina, M., Giannini, N., Bertelli, S., . . . Boyd, C. A. (2007). Paleogene equatorial penguins challenge the proposed relationship between biogeography, diversity, and Cenozoic climate change. *Proceedings of the National Academy of Sciences of the United States of America, 104*(28), 11545–11550. https://doi.org/10.1073/pnas.0611099104

Clift, P., & Vannucchi, P. (2004). Controls on tectonic accretion versus erosion in subduction zones: Implications for the origin and recycling of the continental crust. *Reviews of Geophysics, 42*(2), 2003RG000127. https://doi.org/10.1029/2003RG000127

Clift, P. D., Pecher, I., Kukowski, N., & Hampel, A. (2003). Tectonic erosion of the Peruvian forearc, Lima Basin, by subduction and Nazca Ridge collision. *Tectonics, 22*(3), 2002TC001386. https://doi.org/10.1029/2002TC001386

Coenen, J. J., Barron, J. A., & DeVries, T. J. (2025). Uppermost Oligocene and Miocene diatom biostratigraphy of Ocean Drilling Program Sites 682 and 688 from the Peru Margin. https://doi.org/10.29041/strat.22.3.01

Coletti, G., Bosio, G., Collareta, A., Malinverno, E., Bracchi, V. A., Di Celma, C., . . . Bianucci, G. (2019). Biostratigraphic, evolutionary, and paleoenvironmental significance of the southernmost lepidocyclinids of the Pacific coast of South America (East Pisco Basin, southern Peru). *Journal of South American Earth Sciences, 96*, 102372. https://doi.org/10.1016/j.jsames.2019.102372

Coletti, G., Mariani, L., Malinverno, E., Vimercati, A., Di Celma, C., Collareta, A., . . . Bosio, G. (2026). A window into a middle Eocene mesotrophic mixed siliciclastic-carbonate system from the South American Pacific margin (Paracas Formation, Pisco Basin, Peru). *Journal of South American Earth Sciences, 174*, 105983. https://doi.org/10.1016/j.jsames.2026.105983

Collareta, A., Tejada Medina, L. M., Chacaltana Budiel, C., Landini, W., Altamirano Sierra, A., Urbina Schmitt, M. & Bianucci, G. (2020). A rhinopristiform sawfish (genus *Pristis*) from the middle Eocene (Lutetian) of southern Peru and its regional implications. *Carnets de Geologie*, *20*(5), 91–105. https://doi.org/10.4267/2042/70759

Collareta, A., Lambert, O., Marx, F. G., de Muizon, C., Varas-Malca, R., Landini, W., . . . Urbina, M. (2021). Vertebrate palaeoecology of the Pisco Formation (Miocene, Peru): Glimpses into the ancient Humboldt Current ecosystem. *Journal of Marine Science and Engineering, 9*(11), 1188. https://doi.org/10.3390/jmse9111188

Coxall, H. K., & Pearson, P. N. (2007). *The Eocene-Oligocene transition, Deep Time Perspect. Clim. Chang. Marrying Signal From Comput. Model. Biol. Proxies* (pp. 351–387). London, UK: The Micropalaeontological Society, Special Publications, The Geological Society.

Coxall, H. K., & Wilson, P. A. (2011). Early Oligocene glaciation and productivity in the eastern equatorial Pacific: Insights into global carbon cycling. *Paleoceanography, 26*(2), PA2221. https://doi.org/10.1029/2010PA002021

Coxall, H. K., Wilson, P. A., Pälike, H., Lear, C. H., & Backman, J. (2005). Rapid stepwise onset of Antarctic glaciation and deeper calcite compensation in the Pacific Ocean. *Nature, 433*(7021), 53–57. https://doi.org/10.1038/nature03135

Davies, A., Kemp, A. E., & Pike, J. (2009). Late Cretaceous seasonal ocean variability from the Arctic. *Nature, 460*(7252), 254–258. https://doi.org/10.1038/nature08141

Davies, A., & Kemp, A. E. (2016). Late Cretaceous seasonal palaeoclimatology and diatom palaeoecology from laminated sediments. *Cretaceous Research, 65*, 82–111. https://doi.org/10.1016/j.cretres.2016.04.014

de Muizon, C., Bianucci, G., Martínez-Cáceres, M., & Lambert, O. (2019). Mystacodon selenensis, the earliest known toothed mysticete (Cetacea, Mammalia) from the late Eocene of Peru: Anatomy, phylogeny, and feeding adaptations. *Geodiversitas, 41*(1), 401–499. https://doi.org/10.5252/geodiversitas2019v41a11

DeVries, T. J. (1998). Oligocene deposition and Cenozoic sequence boundaries in the Pisco Basin (Peru). *Journal of South American Earth Sciences, 11*(3), 217–231. https://doi.org/10.1016/S0895-9811(98)00014-5

DeVries, T. J. (2017). Eocene stratigraphy and depositional history near puerto Caballas (East Pisco Basin, Peru). *Boletín de la Sociedad Geológica del Perú, 112*, 39–52.

DeVries, T. J. (2019). Early Paleogene brackish-water molluscs from the Caballas Formation of the East Pisco Basin (southern Peru). *Journal of Natural History, 53*(25–26), 1533–1584. https://doi.org/10.1080/00222933.2018.1524032

DeVries, T. J., & Jud, N. A. (2018). Lithofacies patterns and paleogeography of the Miocene Chilcatay and lower Pisco depositional sequences (East Pisco Basin, Peru). *Boletín de la Sociedad Geológica del Perú, 8*, 124–167.

DeVries, T.J., Narvaez, Y., Sanfilippo, A., Malumian, N., & Tapia, P. (2006). New microfossil evidence for a late Eocene age of the Otuma formation (Southern Peru) XIII Congreso Peruano de Geología, Lima, Peru, October, 2006. Sociedad Geológica del Perú, Publicacíon Especial, pp. 615–618.

DeVries, T. J., Urbina, M., & Jud, N. A. (2017). The Eocene-Oligocene Otuma depositional sequence (East Pisco Basin, Peru): Paleogeographic and paleoceanographic implications of new data. *Boletín de la Sociedad Geológica del Perú, 112*, 14–38.

DeVries, T. J., Barron, J. A., Urbina-Schmitt, M., Ochoa, D., Esperante, R., & Snee, L. W. (2021). The Miocene stratigraphy of the Laberinto area (Río Ica Valley) and its bearing on the geological history of the East Pisco Basin (south-central Peru). *Journal of South American Earth Sciences, 111*, 103458. https://doi.org/10.1016/j.jsames.2021.103458

DeVries, T. J., Barron, J. A., Ochoa, D., & McDougall, K. (2024). Chronology and Paleoenvironment of the Tunga Formation, a new lowermostMiocene sequence in the East Pisco Basin of southern Peru. *Stratigraphy, 21*(3), 189–224.

Di Celma, C., Malinverno, E., Bosio, G., Collareta, A., Gariboldi, K., Gioncada, A., . . . Bianucci, G. (2017). Sequence stratigraphy and paleontology of the Upper Miocene Pisco Formation along the western side of the lower Ica Valley (Ica Desert, Peru). *Rivista Italiana di Paleontologia e Stratigrafia, 123*(2), 255–273.

Di Celma, C., Malinverno, E., Collareta, A., Bosio, G., Gariboldi, K., Lambert, O., . . . Bianucci, G. (2018a). Facies analysis, stratigraphy and marine vertebrate assemblage of the lower Miocene Chilcatay Formation at Ullujaya (Pisco basin, Peru). *Journal of Maps, 14*(2), 257–268. https://doi.org/10.1080/17445647.2018.1456490

Di Celma, C., Malinverno, E., Bosio, G., Gariboldi, K., Collareta, A., Gioncada, A., . . . Bianucci, G. (2018b). Intraformational unconformities as a record of late Miocene eustatic falls of sea level in the Pisco Formation (southern Peru). *Journal of Maps, 14*(2), 607–619. https://doi.org/10.1080/17445647.2018.1517701

Di Celma, C., Pierantoni, P. P., Volatili, T., Molli, G., Mazzoli, S., Sarti, G., . . . Bianucci, G. (2022). Towards deciphering the Cenozoic evolution of the East Pisco Basin (southern Peru). *Journal of Maps, 18*(2), 397–412. https://doi.org/10.1080/17445647.2022.2072780

Diester-Haass, L., & Zachos, J. C. (2003). The Eocene-Oligocene transition in the Equatorial Atlantic (ODP Site 925); Paleoproductivity increase and positive δ13C excursion. In D. R. Prothero, L. C. Ivany, & E. A. Nesbitt (Eds.), *From Greenhouse to Icehouse; The Marine Eocene-Oligocene Transition* (pp. 397–416). New York, NY, USA: Columbia Univ. Press.

Dunbar, R. B., Marty, R. C., & Baker, P. A. (1990). Cenozoic marine sedimentation in the Sechura and Pisco basins, Peru. *Palaeogeography, Palaeoclimatology, Palaeoecology, 77*(3–4), 235–261. https://doi.org/10.1016/0031-0182(90)90179-B

Dunkley Jones, T., Bown, P. R., Pearson, P. N., Wade, B. S., Coxall, H. K., & Lear, C. H. (2008). Major shifts in calcareous phytoplankton assemblages through the Eocene-Oligocene transition of Tanzania and their implications for low-latitude primary production. *Paleoceanography, 23*(4), 2008PA001640. https://doi.org/10.1029/2008PA001640

Egan, K. E., Rickaby, R. E., Hendry, K. R., & Halliday, A. N. (2013). Opening the gateways for diatoms primes Earth for Antarctic glaciation. *Earth and Planetary Science Letters, 375*, 34–43. https://doi.org/10.1016/j.epsl.2013.04.030

Esperante, R., Brand, L. R., Chadwick, A. V., & Poma, O. (2015). Taphonomy and paleoenvironmental conditions of deposition of fossil whales in the diatomaceous sediments of the Miocene/Pliocene Pisco Formation, southern Peru—A new fossil-lagerstätte. *Palaeogeography, Palaeoclimatology, Palaeoecology, 417*, 337–370. https://doi.org/10.1016/j.palaeo.2014.09.029

Fenner, J. (1978). Cenozoic diatom biostratigraphy of the equatorial and southern Atlantic Ocean. *Initial Reports of the Deep Sea Drilling Project, 38*(40/41, Supl.). https://doi.org/10.2973/dsdp.proc.38394041s.201.1978

Fenner, J. (1984). Eocene-Oligocene planktic diatom stratigraphy in the low latitudes and high southern latitudes. *Micropaleontology, 30*(4), 319–342. https://doi.org/10.2307/1485708

Fenner, J. (1985). Late Cretaceous to Oligocene planktic diatoms. In H. M. Bolli, J. B. Saunders, & K. Perch-Nielsen (Eds.), *Plankton Stratigraphy* (pp. 413–456).

Fenner, J. M. (1991). Taxonomy, stratigraphy, and paleoceanographic implications of Paleocene diatoms. Proceedings of the Ocean Drilling Program, 114 Scientific Reports. https://doi.org/10.2973/odp.proc.sr.114.137.1991

Fildani, A., Hessler, A. M., & Graham, S. A. (2008). Trench-forearc interactions reflected in the sedimentary fill of Talara basin, northwest Peru. *Basin Research, 20*(3), 305–331. https://doi.org/10.1111/j.1365-2117.2007.00346.x

Fornaciari, E., Agnini, C., Catanzariti, R., Rio, D., Bolla, M. E., & Valvasoni, E. (2010). Mid-latitude calcareous nannofossil biostratigraphy and biochronology across the middle to late Eocene transition. *Stratigraphy, 7*(4), 229–264. https://doi.org/10.29041/strat.07.4.01

Fourtanier, E., & Macharé, J. (1988). Late Eocene to Pliocene marine diatoms from Peru. In: Round, F.E. (Ed.), Proc. Ninth Int. Diatom Symp. Bristolpress, Bristol, pp. 151–163.

Gariboldi, K., Gioncada, A., Bosio, G., Malinverno, E., Di Celma, C., Tinelli, C., . . . Bianucci, G. (2015). The do-

lomite nodules enclosing fossil marine vertebrates in the East Pisco Basin, Peru: Field and petrographic insights into the Lagerstätte formation. *Palaeogeography, Palaeoclimatology, Palaeoecology, 438*, 81–95. https://doi.org/10.1016/j.palaeo.2015.07.047

Gombos, A.M. (1976). Paleogene and Neogene diatoms from the Falkland Plateau and Malvinas outer basin: Leg 36, Deep Sea Drilling Project. In P. Barker, IWD, Dalziel, M. G. Dinkelman, D. H. Elliott, A. M. Gombos Jr., A. Lonardi, G. Plafker, J. Tarney, R. W. Thomson, R. C. Tjalsma, C. C. von der Borch, S. W. Wise Jr. (Eds.), *Initial Reports of the Deep Sea Drilling Project, 36* (pp. 575–687). U.S. Government Printing Office.

Gradstein, F.M., Ogg, J.G., Smith, A.G., Agterberg, F.P., Bleeker, W., Cooper, R.A., . . . Wilson, D. (2004). A Geologic Time Scale 2004. Cambridge University Press, 500 pp.

Gradstein, F., Ogg, J. G., Schmitz, M. D., & Ogg, G. M. (Eds.). (2012). The geologic time scale 2012. Elsevier.

Gradstein, F. M., & Ogg, J. G. (2020). The chronostratigraphic scale. In *Geologic time scale 2020* (pp. 21–32). Elsevier. https://doi.org/10.1016/B978-0-12-824360-2.00002-4

Griggs, A. J., Davies, S. M., Abbott, P. M., Rasmussen, T. L., & Palmer, A. P. (2014). Optimising the use of marine tephrochronology in the North Atlantic: A detailed investigation of the Faroe Marine Ash Zones II, III and IV. *Quaternary Science Reviews, 106*, 122–139. https://doi.org/10.1016/j.quascirev.2014.04.031

Harwood, D. M., & Bohaty, S. M. (2001). Early Oligocene siliceous microfossil biostratigraphy of Cape Roberts Project core CRP-3, Victoria Land Basin, Antarctica. *Terra Antarctica, 8*(4), 315–338.

Herbozo, G., Kukowski, N., Clift, P. D., Pecher, I., & Bolaños, R. (2020). Cenozoic increase in subduction erosion during plate convergence variability along the convergent margin off Trujillo, Peru. *Tectonophysics, 790*, 228557. https://doi.org/10.1016/j.tecto.2020.228557

Hsu, J. T. (1992). Quaternary uplift of the Peruvian coast related to the subduction of the Nazca Ridge: 13.5 to 15.6 degrees south latitude. *Quaternary International, 15–16*, 87–97. https://doi.org/10.1016/1040-6182(92)90038-4

Hutchinson, D. K., Coxall, H. K., Lunt, D. J., Steinthorsdottir, M., De Boer, A. M., Baatsen, M., . . . Zhang, Z. (2021). The Eocene–Oligocene transition: A review of marine and terrestrial proxy data, models and model–data comparisons. *Climate of the Past, 17*(1), 269–315. https://doi.org/10.5194/cp-17-269-2021

Iglesias-Rodríguez, M. D., Brown, C. W., Doney, S. C., Kleypas, J., Kolber, D., Kolber, Z., . . . Falkowski, P. G. (2002). Representing key phytoplankton functional groups in ocean carbon cycle models: Coccolithophorids. *Global Biogeochemical Cycles, 16*(4), 1100. https://doi.org/10.1029/2001GB001454

Jahnke, R. A., Craven, D. B., & Gaillard, J. F. (1994). The influence of organic matter diagenesis on CaCO3 dissolution at the deep-sea floor. *Geochimica et Cosmochimica Acta, 58*(13), 2799–2809. https://doi.org/10.1016/0016-7037(94)90115-5

Jousé, A. P. (1973). Diatoms in the Oligocene-Miocene biostratigraphic zones of the tropical areas of the Pacific Ocean. *Beihefte zur Nova Hedwigia, 45*, 333–357.

Kemp, A. E., Pike, J., Pearce, R. B., & Lange, C. B. (2000). The "Fall dump"—A new perspective on the role of a "shade flora" in the annual cycle of diatom production and export flux. *Deep-sea Research. Part II, Topical Studies in Oceanography, 47*(9–11), 2129–2154. https://doi.org/10.1016/S0967-0645(00)00019-9

Kennett, J. P., & Shackleton, N. J. (1976). Oxygen isotopic evidence for the development of the psychrosphere 38 Myr ago. *Nature, 260*(5551), 513–515. https://doi.org/10.1038/260513a0

Koç, N., & Scherer, R.P. (1996). Neogene Diatom Biostratigraphy of the Iceland Sea Site 9071 Proceedings of the Ocean Drilling Program. Sci. Res. 61–74.

Ksepka, D. T., Clarke, J. A., DeVries, T. J., & Urbina, M. (2008). Osteology of *Icadyptes salasi*, a giant penguin from the Eocene of Peru. *Journal of Anatomy, 213*(2), 131–147. https://doi.org/10.1111/j.1469-7580.2008.00927.x

Lajo-Yáñez, J. A., Flint, S. S.,Huuse, M., & Brunt, R. L. (2024).Tectono-stratigraphic insights on thedynamics of a complex subduction zone, northern Peruvian forearc. *Tectonics, 43,* e2023TC007860. https://doi.org/10.1029/2023TC007860.

Lambert, O., Collareta, A., Landini, W., Post, K., Ramassamy, B., Di Celma, C., Urbina-Schmitt, M., & Bianucci, G. (2015). No deep diving: evidence of predation on epipelagic fish for a stem beaked whale from the Late Miocene of Peru. In: Proceedings of the National Academy of Sciences, 282 article #20151530. https://doi.org/10.1098/rspb.2015.1530

Lambert, O., Martinez-Caceres, M., Bianucci, G., Di Celma, C., Salas-Sigismondi, R., Sterbaut, E., . . . de Muizon, C. (2017). Earliest Mysticete from the Late Eocene of Peru Sheds New Light on the Origin of Baleen Whales. *Current Biology : CB, 27*(10), 1–7. https://doi.org/10.1016/j.cub.2017.04.026

Lambert, O., Bianucci, G., Salas-Sigismondi, R., Di Celma, C., Sterbaut, E., Urbina, M., & de Muizon, C. (2019). An Amphibious Whale from the Middle Eocene of Peru Reveals Early South Pacific Dispersal of Quadrupedal Cetaceans. *Current Biology : CB, 29*(8), 1352–1359. https://doi.org/10.1016/j.cub.2019.02.050

Lazarus, D., Barron, J., Renaudie, J., Diver, P., & Türke, A. (2014). Cenozoic planktonic marine diatom diversity and correlation to climate change. *PLoS One, 9*(1), e84857. https://doi.org/10.1371/journal.pone.0084857

Lear, C. H., Bailey, T. R., Pearson, P. N., Coxall, H. K., & Rosenthal, Y. (2008). Cooling and ice growth across the Eocene-Oligocene transition. *Geology, 36*(3), 251–254. https://doi.org/10.1130/G24584A.1

León, W., Rosell, W., Aleman, A., Torres, V., & de la Cruz, O. (2008). *Estratigrafía, sedimentología, y evolución tectónica de la Cuenca Pisco Oriental. Instituto Ge-*

ológico, Minero, y Metalúrgicos, Estudios Regionales, Serie D (Vol. 27). Boletín.

Lowe, D. J. (2011). Tephrochronology and its application: A review. *Quaternary Geochronology, 6*(2), 107–153. https://doi.org/10.1016/j.quageo.2010.08.003

Macharé, J., & Ortlieb, L. (1992). Plio-Quaternary vertical motions and the subduction of the Nazca Ridge, central coast of Peru. *Tectonophysics, 205*(1–3), 97–108. https://doi.org/10.1016/0040-1951(92)90420-B

Malinverno, E., Bosio, G., Di Celma, C., Gariboldi, K., Gioncada, A., Pierantoni, P. P., . . . Bianucci, G. (2021). (Bio) stratigraphic overview and paleoclimatic-paleoceanographic implications of the middle-upper Eocene deposits from the Ica River Valley (East Pisco Basin, Peru). *Palaeogeography, Palaeoclimatology, Palaeoecology, 578*, 110567. https://doi.org/10.1016/j.palaeo.2021.110567

Malinverno, E., Bosio, G., Gastaldello, M. E., Pellegrino, L., Bianucci, G., Collareta, A., . . . Di Celma, C. (2025). The early depositional history of the Pisco Formation (Miocene, Peru). *Newsletters on Stratigraphy, 58*(1), 99–123. https://doi.org/10.1127/nos/2025/0864

Marino, M., & Flores, J. A. (2002). Middle Eocene to early Oligocene calcareous nannofossil stratigraphy at Leg 177 Site 1090. *Marine Micropaleontology, 45*(3–4), 383–398. https://doi.org/10.1016/S0377-8398(02)00036-1

Martínez-Cáceres, M., & de Muizon, C. (2011). A new basilosaurid (Cetacea, Pelagiceti) from the late Eocene to early Oligocene Otuma Formation of Peru. *Comptes Rendus. Palévol, 10*(7), 517–526. https://doi.org/10.1016/j.crpv.2011.03.006

Martínez-Cáceres, M., Lambert, O., & de Muizon, C. (2017). The anatomy and phylogenetic affinities of Cynthiacetus peruvianus, a large Dorudon-like basilosaurid (Cetacea, Mammalia) from the late Eocene of Peru. *Geodiversitas, 39*(1), 7–163. https://doi.org/10.5252/g2017n1a1

Martini, E. (1971). Standard Tertiary and Quaternary calcareous nannoplankton zonation. In: Farinacci, A. (Ed.), Proceedings 2nd International Conference Planktonic Microfossils. Tecnosci, Rome, pp. 739–785. Roma. Ed.

Marty, R., Dunbar, R., Martin, J. B., & Baker, P. (1988). Late Eocene diatomite from the Peruvian coastal desert, coastal upwelling in the eastern Pacific, and Pacific circulation before the terminal Eocene event. *Geology, 16*(9), 818–822. https://doi.org/10.1130/0091-7613(1988)0162.3.CO;2

McCartney, K., Witkowski, J., Nowakowski, R., Szaruga, A., Wróbel, R., & Zgłobicka, I. (2020). Evolution of the silicoflagellate naviculopsid skeletal morphology in the Cenozoic. *Marine Micropaleontology, 156*, 101820. https://doi.org/10.1016/j.marmicro.2019.101820

McKay, R. M. L., Villareal, T. A., & La Roche, J. (2000). Vertical migration by Rhizosolenia spp.(Bacillariophyceae): Implications for Fe acquisition. *Journal of Phycology, 36*(4), 669–674. https://doi.org/10.1046/j.1529-8817.2000.99125.x

Miller, K. G., Wright, J. D., & Fairbanks, R. G. (1991). Unlocking the ice house: Oligocene-Miocene oxygen isotopes, eustasy, and margin erosion. *Journal of Geophysical Research, 96*(B4), 6829–6848. https://doi.org/10.1029/90JB02015

Miller, K. G., Wright, J. D., Katz, M. E., Wade, B. S., Browning, J. V., Cramer, B. S., & Rosenthal, Y. (2009). Geological Society of America Special Papers: *Vol. 452. Climate threshold at the Eocene-Oligocene transition: Antarctic ice sheet influence on ocean circulation* (pp. 169–178).

Nyerges, A., Kocsis, Á. T., & Pálfy, J. (2021). Changes in calcareous nannoplankton assemblages around the Eocene-Oligocene climate transition in the Hungarian Palaeogene Basin (Central Paratethys). *Historical Biology, 33*(9), 1443–1456. https://doi.org/10.1080/08912963.2019.1705295

Okada, H., & Bukry, D. (1980). Supplementary modification and introduction of code numbers to the low-latitude coccolith biostratigraphic zonation (Bukry 1973, 1975). *Marine Micropaleontology, 5*, 321–325. https://doi.org/10.1016/0377-8398(80)90016-X

Oreshkina, T. V., & Radionova, E. P. (2014). Diatom record of the Paleocene–Eocene Thermal Maximum in marine paleobasins of Central Russia, Transuralia and adjacent regions. *Nova Hedwigia. Beiheft, 143*, 307–336.

Özen, V., Renaudie, J., & Lazarus, D. (2026). Unraveling Southern Ocean diatom diversity across the Eocene–Oligocene transition. *Journal of Micropalaeontology*, *45*(1), 177–194.

Pälike, H., Norris, R. D., Herrle, J. O., Wilson, P. A., Coxall, H. K., Lear, C. H., . . . Wade, B. S. (2006). The heartbeat of the Oligocene climate system. *Science, 314*(5807), 1894–1898. https://doi.org/10.1126/science.1133822

Pälike, H., Lyle, M. W., Nishi, H., Raffi, I., Ridgwell, A., Gamage, K., . . . Zeebe, R. E. (2012). A Cenozoic record of the equatorial Pacific carbonate compensation depth. *Nature, 488*(7413), 609–614. https://doi.org/10.1038/nature11360

Patacci, M. (2016). A high-precision Jacob's staff with improved spatial accuracy and laser sighting capability. *Sedimentary Geology, 335*, 66–69. https://doi.org/10.1016/j.sedgeo.2016.02.001

Perch-Nielsen, K. (1985a). Cenozoic calcareous nannofossils. In H. M. Bolli, J. B. Saunders, & K. Perch-Nielsen (Eds.), *Plankton Stratigraphy* (pp. 427–554). Cambridge Earth Science Series.

Perch-Nielsen, K. (1985b). Silicoflagellates. In H. M. Bolli, J. B. Saunders, & K. Perch-Nielsen (Eds.), *Plankton Stratigraphy* (pp. 811–846). Cambridge Earth Science Series.

Persico, D., & Villa, G. (2004). Eocene–Oligocene calcareous nannofossils from Maud Rise and Kerguelen Plateau (Antarctica): Paleoecological and paleoceanographic implications. *Marine Micropaleontology, 52*(1–4), 153–179. https://doi.org/10.1016/j.marmicro.2004.05.002

Peterson, L. C., & Prell, W. L. (1985). Carbonate dissolution in recent sediments of the eastern equatorial Indian Ocean: Preservation patterns and carbonate loss above

the lysocline. *Marine Geology, 64*(3–4), 259–290. https://doi.org/10.1016/0025-3227(85)90108-2

Prothero, D. R., & Berggren, W. A. (1992). *Eocene-Oligocene Climatic and Biotic Evolution*. Princeton, NJ, USA: Princeton University Press. https://doi.org/10.1515/9781400862924

Quispe, K., Baby, P., Calderón, Y., Hurtado, C., & Ramírez, L. (2018). La cuenca Pisco: Nuevo modelo estructural para una cuenca de antearco peruana, evidencias de contextos compresivo y distensivo, desarollo de la Cordillera de la Costa. www.sgp.org.pe ISSN 0079-1091.

Renaudie, J. (2016). Quantifying the Cenozoic marine diatom deposition history: Links to the C and Si cycles. *Biogeosciences, 13*(21), 6003–6014. https://doi.org/10.5194/bg-13-6003-2016

Romero, D., Valencia, K., Alarcón, P., Peña, D., & Ramos, V. A. (2013). The offshore basement of Perú: Evidence for different igneous and metamorphic domains in the forearc. *Journal of South American Earth Sciences, 42*, 47–60. https://doi.org/10.1016/j.jsames.2012.11.003

Saillard, M., Hall, S.R., Audin, L., Faber, D.L., Regard, V., & Herail, G. (2011). Andean coastal uplift and active tectonics in southern Peru: Be-10 surface exposure dating of differentially uplifted marine terrace sequences (San Juan de Marcona, similar to 15.4 degrees S). *Geomorphology, 128*, 178–190. https://doi.org/10.1016/j.geomorph.2011.01.004

Scherer, R. P., Gladenkov, A. Y., & Barron, J. A. (2007). Methods and applications of Cenozoic marine diatom biostratigraphy. *The Paleontological Society Papers, 13*, 61–83. https://doi.org/10.1017/S1089332600001467

Schulte, S., & Bard, E. (2003). Past changes in biologically mediated dissolution of calcite above the chemical lysocline recorded in Indian Ocean sediments. *Quaternary Science Reviews, 22*(15–17), 1757–1770. https://doi.org/10.1016/S0277-3791(03)00172-0

Shackleton, N. J., & Kennett, J. P. (1975). Paleotemperature history of the Cenozoic and the initiation of Antarctic glaciation: Oxygen and carbon isotope analyses in DSDP Sites 277, 279 and 281. Deep Sea Drilling Project. *Initial Reports, 29*, 743–755.

Sims, P. A., Fryxell, G., & Baldauf, J. G. (1989). Critical examination of the diatom genus Azpeitia; species useful as biostratigraphic markers for the Oligocene and Miocene epochs. *Micropaleontology, 35*(4), 293–307. https://doi.org/10.2307/1485673

Śliwińska, K. K., Coxall, H. K., Hutchinson, D. K., Liebrand, D., Schouten, S., & de Boer, A. M. (2023). Sea surface temperature evolution of the North Atlantic Ocean across the Eocene–Oligocene transition. *Climate of the Past, 19*(1), 123–140. https://doi.org/10.5194/cp-19-123-2023

Stern, C. R. (2011). Subduction erosion: Rates, mechanisms, and its role in arc magmatism and the evolution of the continental crust and mantle. *Gondwana Research, 20*(2–3), 284–308. https://doi.org/10.1016/j.gr.2011.03.006

Strelnikova, N.I., Fourtanier, E., Kociolek, J.P., & Barron, J.A. (2001). Ultrastructure studies of Coscinodiscus and Cestodiscus species from the Eocene and Oligocene. In: Lange-Bertalot Fest Schrift. Studies on Diatoms. Dedicated to prof. Dr. hc Horst Lange-Bertalot On the occasion of his 65th Birthday, pp. 63–96.

Sun, J., Ni, X., Bi, S., Wu, W., Ye, J., Meng, J., & Windley, B. F. (2014). Synchronous turnover of flora, fauna and climate at the Eocene–Oligocene Boundary in Asia. *Scientific Reports, 4*(1), 7463. https://doi.org/10.1038/srep07463

Suess, E., von Huene, R., Shipboard Scientific Party Site 681 (1988). Proceedings of the Ocean Drilling Program 112, Scientific Results, Initial Reports, College Station, TX (Ocean Drilling Program) (1988), pp. 305–363.

Suto, I., Kawamura, K., Hagimoto, S., Teraishi, A., & Tanaka, Y. (2012). Changes in upwelling mechanisms drove the evolution of marine organisms. *Palaeogeography, Palaeoclimatology, Palaeoecology, 339–341*, 39–51. https://doi.org/10.1016/j.palaeo.2012.04.014

Toffanin, F., Agnini, C., Rio, D., Acton, G., & Westerhold, T. (2013). Middle Eocene to early Oligocene calcareous nannofossil biostratigraphy at IODP Site U1333 (equatorial Pacific). *Micropaleontology, 59*(1), 69–82. https://doi.org/10.47894/mpal.59.1.04

Tozzi, S., Schofield, O., & Falkowski, P. (2004). Historical climate change and ocean turbulence as selective agents for two key phytoplankton functional groups. *Marine Ecology Progress Series, 274*, 123–132. https://doi.org/10.3354/meps274123

Uhen, M. D., Pyenson, N. D., Devries, T. J., Urbina, M., & Renne, P. R. (2011). New middle Eocene whales from the Pisco Basin of Peru. *Journal of Paleontology, 85*(5), 955–969. https://doi.org/10.1666/10-162.1

Viganò, A., Coxall, H. K., Holmström, M., Vinco, M., Lear, C. H., & Agnini, C. (2023). Calcareous nannofossils across the Eocene-Oligocene transition at Site 756 (Ninetyeast Ridge, Indian Ocean): Implications for biostratigraphy and paleoceanographic clues. *Newsletters on Stratigraphy, 56*(2), 187–223. https://doi.org/10.1127/nos/2022/0725

Viganò, A., Dallanave, E., Alegret, L., Westerhold, T., Sutherland, R., Dickens, G. R., Newsam, C., & Agnini, C. (2024). Calcareous nannofossils and paleoclimatic evolution across the Eocene-Oligocene transition at IODP Site U1509, Tasman Sea, Southwest Pacific Ocean. *Paleoceanography and Paleoclimatology, 39*(2), e2023PA004738.

Viganò, A., & Agnini, C. (2025). Beyond the ice: Shifts in productivity and carbonate oversaturation at the Eocene–Oligocene transition. *Scientific Reports, 15*(1), 15281. https://doi.org/10.1038/s41598-025-99630-4

Villa, G., Fioroni, C., Pea, L., Bohaty, S., & Persico, D. (2008). Middle Eocene–late Oligocene climate variability: Calcareous nannofossil response at Kerguelen Plateau, Site 748. *Marine Micropaleontology, 69*(2), 173–192. https://doi.org/10.1016/j.marmicro.2008.07.006

Villa, G., Fioroni, C., Persico, D., Roberts, A. P., & Florindo, F. (2014). Middle Eocene to late Oligocene Antarctic glaciation/deglaciation and Southern Ocean pro-

ductivity. *Paleoceanography, 29*(3), 223–237. https://doi.org/10.1002/2013PA002518

Villa, I. M., & Bosio, G. (2023). "Excess Ar" by laboratory alteration of biotite. *Geology, 51*(1), 121–125. https://doi.org/10.1130/G50503.1

Viveen, W., & Schlunegger, F. (2018). Prolonged extension and subsidence of the Peruvian forearc during the Cenozoic. *Tectonophysics, 730*, 48–62. https://doi.org/10.1016/j.tecto.2018.02.018

von Huene, R., & Suess, E. (1988). Ocean Drilling Program Leg 112, Peru continental margin: Part 1, tectonic history. *Geology, 16*(10), 934–938. https://doi.org/10.1130/0091-7613(1988)0162.3.CO;2

von Huene, R., & Lallemand, S. (1990). Tectonic erosion along the Japan and Peru convergent margins. *Geological Society of America Bulletin, 102*(6), 704–720. https://doi.org/10.1130/0016-7606(1990)1022.3.CO;2

Wade, B. S., & Bown, P. R. (2006). Calcareous nannofossils in extreme environments: The Messinian salinity crisis, Polemi Basin, Cyprus. *Palaeogeography, Palaeoclimatology, Palaeoecology, 233*(3–4), 271–286. https://doi.org/10.1016/j.palaeo.2005.10.007

Wade, B. S., Houben, A. J., Quaijtaal, W., Schouten, S., Rosenthal, Y., Miller, K. G., . . . Brinkhuis, H. (2012). Multiproxy record of abrupt sea-surface cooling across the Eocene-Oligocene transition in the Gulf of Mexico. *Geology, 40*(2), 159–162. https://doi.org/10.1130/G32577.1

Wade, B. S., O'Neill, J. F., Phujareanchaiwon, C., Ali, I., Lyle, M., & Witkowski, J. (2020). Evolution of deep-sea sediments across the Paleocene-Eocene and Eocene-Oligocene boundaries. *Earth-Science Reviews*, *211*, 103403. https://doi.org/10.1016/j.earscirev.2020.103403

Wenzhöfer, F., Adler, M., Kohls, O., Hensen, C., Strotmann, B., Boehme, S., & Schulz, H. D. (2001). Calcite dissolution driven by benthic mineralization in the deep-sea: In situ measurements of Ca2+, pH, pCO2 and O2. *Geochimica et Cosmochimica Acta, 65*(16), 2677–2690. https://doi.org/10.1016/S0016-7037(01)00620-2

Westerhold, T., Marwan, N., Drury, A. J., Liebrand, D., Agnini, C., Anagnostou, E., . . . Zachos, J. C. (2020). An astronomically dated record of Earth's climate and its predictability over the last 66 million years. *Science, 369*(6509), 1383–1387. https://doi.org/10.1126/science.aba6853

Young, J. R., Bown, P. R., & Lees, J. A. (2024). Nannotax3 website. International Nannoplankton Association. Accessed 21 Nov. 2024. URL. http://www.mikrotax.org/Nannotax3

Zachos, J. C., Dickens, G. R., & Zeebe, R. E. (2008). An early Cenozoic perspective on greenhouse warming and carbon-cycle dynamics. *Nature, 451*(7176), 279–283. https://doi.org/10.1038/nature06588

Zachos, J. C., Quinn, T. M., & Salamy, K. A. (1996). High-resolution (104 years) deep-sea foraminiferal stable isotope records of the Eocene-Oligocene climate transition. *Paleoceanography, 11*(3), 251–266. https://doi.org/10.1029/96PA00571

Manuscript received: February 14, 2025
Accepted: March 22, 2026

Table of contents – Electronic Supplementary Material (ESM)

Supplementary Table S1 and S2

The pdf version of this paper includes an electronic supplement
Please save the electronic supplement contained in this pdf-file by clicking the blue frame above. After saving rename the file extension to .zip (for security reasons Adobe does not allow to embed .exe, .zip, .rar etc. files).